PNNL-36408

Studies on Printability Methodologies and Directed-Energy-Deposition-Fabricated Iron Alloys for Nuclear Applications

August 2024

Subhashish Meher
Asif Mahmud
Chinthaka Silva
Ariel Rieffer
Isabella J van Rooyen
Ankit Roy
Peter A Renner
Mohan SKKY Nartu
German A Valenzuela

M3CT-24PN1304051

Prepared for the U.S. Department of Energy
under Contract DE-AC05-76RL01830

PACIFIC NORTHWEST NATIONAL LABORATORY
operated by
BATTELLE
for the
UNITED STATES DEPARTMENT OF ENERGY
under Contract DE-AC05-76RL01830

Printed in the United States of America

Available to DOE and DOE contractors from the
Office of Scientific and Technical Information,
P.O. Box 62, Oak Ridge, TN 37831-0062;
ph: (865) 576-8401
fax: (865) 576-5728
email: reports@adonis.osti.gov

Available to the public from the National Technical Information Service
5301 Shawnee Rd., Alexandria, VA 22312
ph: (800) 553-NTIS (6847)
email: orders@ntis.gov <https://www.ntis.gov/about>
Online ordering: http://www.ntis.gov

PNNL-36408

Studies on Printability Methodologies and Directed-Energy-Deposition-Fabricated Iron Alloys for Nuclear Applications

August 2024

Subhashish Meher
Asif Mahmud
Chinthaka Silva
Ariel Rieffer
Isabella J van Rooyen
Ankit Roy
Peter A Renner
Mohan SKKY Nartu
German A Valenzuela

M3CT-24PN1304051

Prepared for
the U.S. Department of Energy
under Contract DE-AC05-76RL01830

Pacific Northwest National Laboratory
Richland, Washington 99354

Summary

This report provides results from a printability study of laser directed energy deposition (DED)-based additive manufacturing of nuclear-grade stainless steels as well as DED process parameter development for austenitic Alloy 709 (A709) and ferritic/martensitic Grade 91 (G91) and Grade 92 (G92) steels. The printability study includes the use of machine learning and physics-based modeling via commercial software such as FLOW-3D for insights into the impact of the alloy composition, particularly the carbon content, on the printability of stainless steels during the DED process.

In the DED process development work, 1 cm^3 alloy blocks were deposited with broad ranges of laser powers, scan speeds, and hatch spacings to optimize the build quality, resulting in densities of more than 99.8% for all three alloys. The microstructure and mechanical properties were characterized using electron microscopy, X-ray diffraction, and Vickers hardness measurements. Further, tensile samples were extracted from DED-fabricated alloys utilizing the optimized process parameters. The present work provides guidance and progress towards the successful deployment of the DED process for the fabrication of structural components of nuclear reactors.

Acknowledgments

The research presented here was supported by the Advanced Materials and Manufacturing Technology (AMMT) program of the U.S. Department of Energy (DOE), Office of Nuclear Energy. Pacific Northwest National Laboratory (PNNL) is a multiprogram national laboratory operated for the DOE by Battelle Memorial Institute under Contract No. DE-AC05-76RL01830. We would like to acknowledge Prof. Xiaoyuan Lou and PhD students John Snitzer and Qianwen Zhang from Purdue University for the laser directed energy deposition of A709, Grade 91, and Grade 92 alloys on behalf of PNNL. We would like to acknowledge Stephanie Barbara Lawson (PhD student), Somayeh Pasebani (Professor) at Oregon State University for their support in the use of Flow-3D software for printability study. We express our gratitude to Carolyn A. Burns for peer-reviewing this report.

Acronyms and Abbreviations

A709	Alloy 709
AM	Additive Manufacturing
AMMT	Advanced Materials and Manufacturing Technologies
Argonne	Argonne National Laboratory
BCC	Body-Centered Cubic
BCT	Body-Centered Tetragonal
BSE	Backscattered Electron
DED	Directed Energy Deposition
DOE	U.S. Department of Energy
EBSD	Electron Backscatter Diffraction
F/M	Ferritic/Martensitic
FCC	Face-Centered Cubic
FIB	Focused Ion Beam
G91	Grade 91
G92	Grade 92
GBR	Gradient Boost Regressor
HEA	High Entropy Alloy
LC	Laser Cladding
LPBF	Laser Powder Bed Fusion
MAE	Mean Absolute Error
ML	Machine Learning
MSE	Mean Squared Error
NE	Office of Nuclear Energy
NN	Neural Network
OM	Optical Microscope
OSU	Oregon State University
PNNL	Pacific Northwest National Laboratory
PMFR	Powder Mass Flow Rate
ReLU	Rectified Linear Unit
RF	Random Forest
RFR	Random Forest Regressor
RMSE	Root Mean Squared Error
SEM	Scanning Electron Microscope
SHAP	Shapley Additive Explanations
SLM	Selective Laser Melting
XRD	X-ray Diffraction

Contents

Figures

Tables

1.0 Introduction

The vision of the “*advanced materials and manufacturing*” effort of the U.S. Department of Energy (DOE), Office of Nuclear Energy (NE), Advanced Materials and Manufacturing Technologies (AMMT) program is to develop materials that can realize a higher thermal efficiency and power output for nuclear reactors, thereby extending their life cycle. The objective of this research effort is to develop a materials design and development approach by integrating modeling and simulation with laser directed energy deposition (DED) additive manufacturing (AM) and characterization. The printability study using machine learning is a continuation of FY-23 and the work in FY-24 is focused on composition effects on printability of 316 L and 316 H.

A DOE-NE advanced Reactor Technology (ART) material down-selection program recommended Alloy 709 [A709], an advanced austenitic stainless-steel alloy, as a Class A structural material for the Sodium cooled Fast Reactor (SFR) because of its overall superior structural strength advantage (Wang, Hou et al. 2022). An extensive work has been performed on A709 in the wrought form to have it code-qualified, but there is no available literature on the additive manufacturing aspect.

Grade-91 [G91] is broadly used in fossil and nuclear power plants in components operating at temperatures up to ~650°C. This alloy is also included in ASME Boiler and Pressure Vessel (B&PV) Code Section III Division 5. Limited amount of work on DED-AM has been performed to fabricate this alloy to understand the microstructural evolution and mechanical behavior (Hatakeyama, Sawada et al. 2023).

To improve the creep properties of 2nd generation G91 alloy, Grade 92 [G92] steel was developed as a 3rd generation creep-resistant F/M steel with the addition of tungsten and minute amounts of boron. While it has been reported to have better creep properties relative to Grade 91, it has not been code qualified (Abe 2008). As of now, there is no available research on the additive manufacturing of Grade 92 steel.

Under the AMMT program, the laser powder bed fusion (LPBF) research is being carried out for these three alloy at Argonne National Laboratory (ANL). While LPBF is better for small to medium-sized components with high detail and internal features, DED combines a material feed system to place the powder onto the exact spot where the laser will melt the material. This AM method can be easily scaled to extremely large components along with high build rate speeds when compared to conventional LPBF systems. Additionally, DED is better choice for complex geometries and compositional gradients.

This work has been divided into two tasks. Task 1 includes use of machine learning (ML) and physics-based modeling via commercial software such as FLOW-3D to gain insights into the impact of the alloy composition, particularly the carbon content, on the printability of stainless steels during the DED process. The findings underscore the importance of tailored compositional adjustments in optimizing process outcomes and pave the way for further refinement of AM processes. Task 2 includes the development of DED process parameters for A709 and G91 and G92 stainless steels, characterization, and hardness evaluation. It was concluded that the process parameters developed in this study with a range of laser powers and scan speeds successfully printed highly dense products of all three alloys. Subsequently, microhardness measurements indicated a direct relation between the hardness and the laser power. These preliminary characterization results will guide the future heat treatments and tensile testing of these alloys.

2.0 Materials

2.1 Austenitic Steel, A709

Austenitic stainless steels are often used for structural components such as piping or intermediate heat exchangers in nuclear power applications (Li, Zeng et al. 2021). A709 is a highly alloyed austenitic stainless steel, with its composition specification listed in Table 1 (Zhao, Cinbiz et al. 2020). A709 is a candidate for nuclear fuel cladding and structural applications in next-generation sodium-cooled fast reactors due to its improved mechanical properties in harsh environments (e.g., creep and corrosion resistance) at elevated temperatures (500–700°C) compared to those of conventional austenitic stainless steels such as SS304 and SS316 (Alomari, Kumar and Murty 2018, Ding, Yan et al. 2019, Zhao, Cinbiz et al. 2020, Li, Zeng et al. 2021). The high-temperature tensile properties, thermal stability, creep strength, creep-fatigue resistance, sodium compatibility, and weldability for A709 and other stainless steels such as 316H were compared in a previous study (Sham, Bass et al. 2022). A709 exhibits the best overall performance, as illustrated in the property ranking chart in Figure 1.

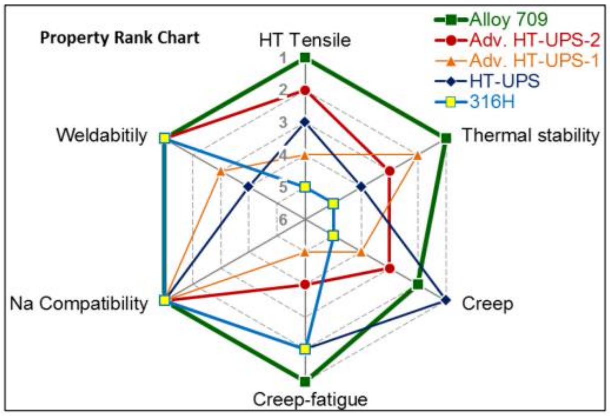

Figure 1. Property ranking chart for A709, HT-UPS, its variants, and Type 316 stainless steels. A709 shows the best overall performance (Sham, Bass et al. 2022).

2.2 Ferritic/Martensitic Steel, Grade 91 and Grade 92

Most of the interest in F/M steels in general is based on the development of next-generation or Generation IV nuclear reactors (Li, Natesan et al. , Armas, Avalos et al. 1998, Seran, Brachet and Alamo 2001, Klueh, Nelson and Oak Ridge National Laboratory 2007, Abe 2008, Shrestha, Alsagabi et al. 2015, Zhou, Liu et al. 2015, Henry and Maloy 2017, Cabet, Dalle et al. 2019, Sridharan and Field 2019, Sridharan, Gussev and Field 2019, Kimura, Kwak et al. 2020, Eftink, Vega et al. 2021, El-Atwani, Eftink et al. 2021, Villaret, Boulnat et al. 2021, Zhong, Sridharan et al. 2021, Feng, Zhang et al. 2022, Sau, Hintsala et al. 2022, Hatakeyama, Sawada et al. 2023, Mantri and Zhang 2023). The development of next-generation or fusion-based energy systems necessitates robust materials capable of withstanding extreme mechanical and thermal conditions, as well as high-energy neutron irradiation (Li, Natesan et al. , Armas, Avalos et al. 1998, Seran, Brachet and Alamo 2001, Klueh, Nelson and Oak Ridge National Laboratory 2007, Abe 2008, Shrestha, Alsagabi et al. 2015, Zhou, Liu et al. 2015, Henry and Maloy 2017, Cabet, Dalle et al. 2019, Sridharan and Field 2019, Sridharan, Gussev and Field 2019, Kimura, Kwak et al. 2020, Eftink, Vega et al. 2021, El-Atwani, Eftink et al. 2021, Villaret, Boulnat et al. 2021, Zhong, Sridharan et al. 2021, Feng, Zhang et al. 2022, Sau, Hintsala et al. 2022, Hatakeyama, Sawada et al. 2023, Mantri and Zhang 2023). F/M steels are known for their strength, oxidation resistance, and suitability for applications in both fusion and fast fission reactors (Shrestha, Alsagabi et al. 2015, Sridharan and Field 2019). Additionally, F/M steels have a higher thermal conductivity, lower expansion coefficient, better creep resistance, radiation tolerance, and better void-swelling resistance compared to those of austenitic stainless steels, making them more desirable for in-core applications such as cladding, wrappers, or ducts (Seran, Brachet and Alamo 2001, Klueh, Nelson and Oak Ridge National Laboratory 2007, Shrestha, Alsagabi et al. 2015, Sridharan and Field 2019). Modified 9Cr–1Mo or G91 and 9Cr–0.5Mo–2W–V, Nb Gr 92: Fe–9Cr–0.5Mo–0.2V–0.05Nb–1.8W or G92 are F/M steels with the composition specifications in Table 1; the variations in composition are slight and generally fall within the same ranges (Klueh, Nelson and Oak Ridge National Laboratory 2007, Shrestha, Alsagabi et al. 2015, Sridharan and Field 2019, ASTM 2023, Hatakeyama, Sawada et al. 2023).

G91 steel is an F/M steel with tempered martensite being the dominant phase. It typically contains 9% chromium, 1% molybdenum, and small amounts of vanadium, niobium, and nitrogen. In addition, the microstructure of G91 steel consists of fine carbides such as $M_{23}C_6$ and MX (M can be V, Nb, etc. and X can be C or N) phases. A heat treatment is often performed on G91 steel in the form of normalizing and tempering, resulting in a refined grain structure that enhances its mechanical properties, as the presence of a minimal amount of δ-ferrite could be detrimental. In general, G91 steel has a high tensile strength and hardness and good creep resistance and fracture toughness.

G92 steel is also an F/M steel with tempered martensite and also contains 9% chromium and 2% tungsten in place of some molybdenum (0.5%), with similar additions of vanadium, niobium, and nitrogen. However, because of the addition of tungsten, it tends to have a more stable carbide distribution and improved thermal stability. G92 steel is subjected to a similar heat treatment as G91 steel; however, its microstructural stability is enhanced because of the addition of tungsten, which forms complex carbides that improve high-temperature performance. For example, the formation of the deleterious δ-ferrite phase is less likely to occur because of the improved carbide stability at high temperatures.

Challenges in manufacturing these steels, particularly in welding and forming complex geometries, have spurred interest in advanced techniques like AM (Cabet, Dalle et al. 2019, Sridharan and Field 2019, Sridharan, Gussev and Field 2019, Zhong, Sridharan et al. 2021), such as laser powder bed fusion (LPBF) and laser DED techniques (Rangaswamy, Griffith et al. 2005, Frazier 2014, Denlinger, Heigel et al. 2015, Gorelik 2017, Romano, Brandao et al. 2017, Li, Liu et al. 2018, Lou, Andresen and Rebak 2018, Poorganji, Ott et al. 2020, Dong, Vecchiato et al. 2021, Singhal, Jain et al. 2023). AM has traditionally been used with common engineering alloys, especially weldable materials, as they are generally seen as good candidates for AM due to the similarities in processes (Singhal, Jain et al. 2023). Steels such as low alloy steel (e.g., 4140), precipitation-hardened steel (e.g., 17-4PH), or most commonly austenitic stainless steel (e.g., 304 or 316) (Rangaswamy, Griffith et al. 2005, Frazier 2014, Li, Liu et al. 2018, Poorganji, Ott et al. 2020, Dong, Vecchiato et al. 2021, Singhal, Jain et al. 2023) have often been used in AM, and within the last five years, research has also included F/M steels (e.g., G91) (Sridharan and Field 2019, Sridharan, Gussev and Field 2019, Eftink, Vega et al. 2021, El-Atwani, Eftink et al. 2021, Zhong, Sridharan et al. 2021, Feng, Zhang et al. 2022, Sau, Hintsala et al. 2022, Hatakeyama, Sawada et al. 2023, Mantri and Zhang 2023). AM is being investigated for its potential to overcome traditional welding limitations, although challenges remain in controlling microstructural transformations and residual stresses (Frazier 2014, Gorelik 2017, Li, Liu et al. 2018, Lou, Andresen and Rebak 2018, Sridharan and Field 2019, Dong, Vecchiato et al. 2021, Eftink, Vega et al. 2021, El-Atwani, Eftink et al. 2021, Villaret, Boulnat et al. 2021, Zhong, Sridharan et al. 2021, Feng, Zhang et al. 2022, Sau, Hintsala et al. 2022, Hatakeyama, Sawada et al. 2023, Mantri and Zhang 2023, Singhal, Jain et al. 2023). In addition, a substantial barrier exists to qualify AM materials for nuclear applications because of the high-risk nature of the application and the lack of experience compared to those fabricated with traditional manufacturing methods (Frazier 2014, Romano, Brandao et al. 2017, Poorganji, Ott et al. 2020). These efforts aim to optimize material properties critical for ensuring structural integrity and performance in next-generation nuclear reactors.

Table 1. Composition specifications of the three alloys selected in this study.

	Fe	Cr	Ni	Mo	Mn	Si	C	N	P	S	Ti	Nb	W	V
A709	Bal.	19.5–23.0	23.0–26.0	1.0–2.0	1.5 max	1 max	0.1 max	0.1–0.25	0.03 max	0.03 max	0.2 max	n/a	n/a	n/a
Grade 91	Bal.	8.3–9	0.17	0.5–1	0.43	0.2	0.1	n/a	n/a	n/a	n/a	0.06	n/a	0.2
Grade 92	Bal.	8.7–9	0.1	0.5–1	0.45	0.2	0.1	n/a	n/a	n/a	n/a	0.07	1.9	0.2

3.0 Printability Study

AM has revolutionized the manufacturing industry by enabling the fabrication of complex geometries with enhanced design flexibility for the aerospace, automotive, and shipping industries (DebRoy, Mukherjee et al. 2019, DebRoy, Mukherjee et al. 2021, Du, Mukherjee and DebRoy 2021, Wei, Mukherjee et al. 2021). Its application in the nuclear engineering field holds significant potential for the development and production of reactor components and materials. Improving the printability of existing reactor alloys using AM techniques can offer substantial benefits in terms of efficiency and performance. Despite heavy research investments in terms of time and cost, only a few commercial alloys that qualify for industrial use can be successfully manufactured by AM, and the market share of these products is currently negligible (Wei, Mukherjee et al. 2021). The small market share of AM products is due to the high probability of formation of defects in AM components due to the lack of fusion, balling, cracking, and porosity (DebRoy, Wei et al. 2018). These defects reduce the dimensional accuracy, which affects the quality and reliability of the parts, thereby requiring post-processing to remove the defects and adding to the cost of production. Most research in the last decade has focused on avoiding these defects by optimizing the process parameters.

The most significant defects identified in literature (Mostafaei, Zhao et al. 2022) are caused by the lack of fusion, keyhole formation, balling, cracking, and trapped gases. These defects contribute to the porosity or a lower relative density (Niu, Li et al. 2020, Yang, Kan et al. 2021). Although experimental work provides reliable and tested data for process optimization and may be practical for a small subset of materials, it is impossible to obtain the processing window for a large set of commercial materials and avoid all practical printing defects in these materials. Under such a circumstance, modeling efforts can prove to be significantly useful. Nanoscale and mesoscale modeling can model AM processes to a high accuracy, but simulations of this nature are computationally intensive both in terms of time and cost. In fact, a molecular dynamics simulation of only a few nanoseconds can cost up to 3 days on 40 cores of high-performance computing (Roy, Munshi and Balasubramanian 2021, Sreeramagiri, Roy and Balasubramanian 2021, Roy, Devanathan et al. 2022, Roy, Singh et al. 2022). Such a computationally intensive approach may not be suitable for the development of a tool for the rapid prediction of defects during AM. A suitable solution to this problem lies in the adoption of ML techniques (Mueller, Kusne and Ramprasad 2016, Butler, Davies et al. 2018). While ML has been widely used for AM problems for the classification of defects, the majority of the ML efforts (Scime and Beuth 2018, Caggiano, Zhang et al. 2019, Zhang, Liu and Shin 2019, Zhang, Soon et al. 2019, Angelone, Caggiano et al. 2020, Baumgartl, Tomas et al. 2020, Li, Jia et al. 2020, Fathizadan, Ju and Lu 2021, Khan, Alam et al. 2021, Snow, Diehl et al. 2021, Westphal and Seitz 2021, Davtalab, Kazemian et al. 2022) have focused on image-based learning and classifying the build quality as defective or acceptable. The methods and findings from these efforts have been summarized in Table 2

Table 2. ML studies on AM defect identification: the dataset, ML models, and accuracy obtained in the identification of defects are summarized.

Ref.	Dataset size and nature	Target application	AM process	Material	Models used	Performance metric (%)
(Caggiano, Zhang et al. 2019)	1,200 images of part slices, 160 × 160 pixels each	Defect condition pattern recognition on scan tracks	Selective laser melting (SLM)	Inconel 780	1	99.4

Ref.	Dataset size and nature	Target application	AM process	Material	Models used	Performance metric (%)
(Scime and Beuth 2018)	10,071 patches from 89 images of 14 builds	Defect type recognition: recoater hopping, recoater streaking, debris, super-elevation, part damage, incomplete spreading	LPBF	AlSi10Mg, bronze, Inconel 625, Inconel 718, stainless steel 316 L, stainless steel 17-4 PH, and Ti-6Al-4V	2	97
(Zhang, Liu and Shin 2019)	~14,200 images	% of porosity	LPBF	Titanium sponge powder	3	91.2
(Zhang, Soon et al. 2019)	~6,000 images	Defect type recognition: overheating, normal, irregularity, balling	LPBF	316 L	3	99.7
(Angelone, Caggiano et al. 2020)	462 images	Defect type recognition: critical stripes, degradation due to faulty powder bed, overmelting,	SLM		3	Critical stripe recognition 87.5, Degradation due to faulty bed = 79.2, Overmelting = 86.1, Recoating defect = 97
(Baumgartl, Tomas et al. 2020)	4,314 RGB color images	Defect type classification: delamination, metal splatters, ok	LPBF	H13 steel	4	96.8
(Khan, Alam et al. 2021)	1,454 images with defects, 241 without defects	Geometric anomalies	Fused filament fabrication		3	85
(Davtalab, Kazemian et al. 2022)	100,000 original images augmented to 1 million images	Bent layers vs. nonbent	Contour crafting		3	97.5
(Snow, Diehl et al. 2021)	9,724 good quality, 2,431 defects	Lack of fusion flaws	LPBF	Ti–6Al–4V	3	93.5
(Li, Jia et al. 2020)	162 images converted into 5,805 training and 1,161 testing samples	Undermelt, overmelt, and good melt	Laser welding	ASTM F75 I CoCrMo	3	95
(Fathizadan, Ju and Lu 2021)	2,824 images for training, 942 for testing	Melt pool quality characterization: anomalous, noisy, and normal	LPBF	Inconel 625	5	95
(Westphal and Seitz 2021)	9,426 images	Cracks, ditches, foreign bodies	Selective laser sintering	Polyamide 12	3	95.8

Although most studies have used ML for defect identification, like porosity, overmelting, lack of fusion, and cracking, by utilizing images of the scan tracks and build morphology, they have only focused on image-based classification of defects. There have only been very few studies that trained physics-based models to predict defect formation and were independent of imaging classification.

The current work is driven by the motivation to possibly reduce balling and porosity defects in existing alloys by minor compositional modifications or fine-tuning the composition by varying the individual components in the allowable concentration range of the alloy. For example, SS316L can have a Ni composition anywhere between 10–14 wt%, which allows an experimentalist to tune its composition by either choosing a lower or higher Ni concentration. The choice of composition at the lower or the higher end of this range of Ni concentrations is easy to make when there is only one variable. However, SS316L has 10 elements (Fe, Cr, Ni, Mo, C, Mn, P, S, Si, and N), all of which can be varied by up to 4 wt% at maximum. Considering such a large number of variables in the composition of the alloy, leveraging ML to investigate the effect of increasing and decreasing the concentration of a specific element or multiple elements simultaneously on the tendency of defect formation of the alloy will be greatly informative for the experimentalist. For given processing conditions, some compositions may produce balling, while the same composition may not encounter balling under different processing conditions. Similarly, the given processing conditions might produce more porosity than other conditions. However, the argument here is that tuning the composition in a way that minimizes balling and porosity under given processing conditions will widen the process window and make it less likely for defects to occur because of local changes in the heat dissipation characteristics when the printing geometry changes, even under constant processing conditions.

To address the defined problem for balling, we trained and tested three ML models in a 32-dimensional design space comprising 26 elemental descriptors and 6 process parameters. The models were trained on a dataset with the 32 descriptors with the output 0 meaning no balling or 1 meaning occurrence of a balling defect similar to that in (Du, Mukherjee and DebRoy 2021). Three types of models, the random forest (RF) classifier, gradient boost regressor (GBR), and neural network (NN) regressor, were trained and tested on the balling datasets, and their performance is compared. To model the porosity defect, we trained and tested three ML models in a 39-dimensional design space comprising 24 element descriptors, 12 element properties, and 3 process parameters. The models were trained on the 39 descriptors with an output in percentage, or the difference between the maximum and relative densities (Chen, Wei et al. 2017). A new model, the random forest regressor (RFR), was used along with the previous GBR and NN regressor. These models were trained, and their error values compared. Some important descriptors and their role in defect formation are discussed subsequently.

To rigorously validate the predictions and insights derived from our ML models, we plan to conduct detailed FLOW-3D simulations focusing on the SS316L and SS316H alloys. These simulations will enable a high-fidelity examination of the melt pool dynamics, solidification patterns, and defect formation mechanisms under various processing conditions. By integrating the thermophysical properties and compositional dependencies into the FLOW-3D framework, we aim to substantiate our hypothesis on the role of compositional fine-tuning in mitigating balling and porosity defects. The outcomes from these simulations will provide a deeper mechanistic understanding and reinforce the robustness of the ML-driven predictive models, ultimately guiding the optimization of process parameters and alloy compositions for enhanced printability and defect minimization.

3.1 Methods

3.1.1 Data Collection and Data Analysis

The dataset in (Du, Mukherjee and DebRoy 2021) is leveraged to build a customized dataset with the new descriptors defined in order to introduce the concentrations of the individual elements in the learning algorithm. In addition to data for 166 alloys from (Du, Mukherjee and DebRoy 2021), data for 101 high entropy alloys (HEAs) and their tendencies to produce balling defects during AM were also collected from literature. A combined dataset of 267 alloys was built, as shown in Figure 2. The HEA data were collected from (Li, Niu et al. 2018, Sarswat, Sarkar et al. 2019, Zhou, Yuan et al. 2019, Sun, Peng et al. 2020, Atli, Boon et al. 2021, Hou, Su et al. 2021, Ikeda, Yonehara et al. 2021, Niu, Li et al. 2021, Gu, Qi et al. 2022, Zhang, Zhou et al. 2022, Mahmood, Alabtah et al. 2023, Tang, Zhang et al. 2023, Wang, Yuan et al. 2023).

For the porosity, the dataset was collected from the literature and from experiments at ANL. The SS316 data provided to us by Argonne have not been shared at this time, as it is part of ongoing research. Data for 138 alloys were collected from the literature (Aboulkhair, Everitt et al. 2014, Attar, Calin et al. 2014, Gong, Rafi et al. 2015, Chen, Wei et al. 2017, Fousova, Vojtech et al. 2017, Enneti, Morgan and Atre 2018, Zhou, Yuan et al. 2019, Adjamskyi, Kononenko and Podolskyi 2020, Lashgari, Xue et al. 2020, Yang, Kan et al. 2021).

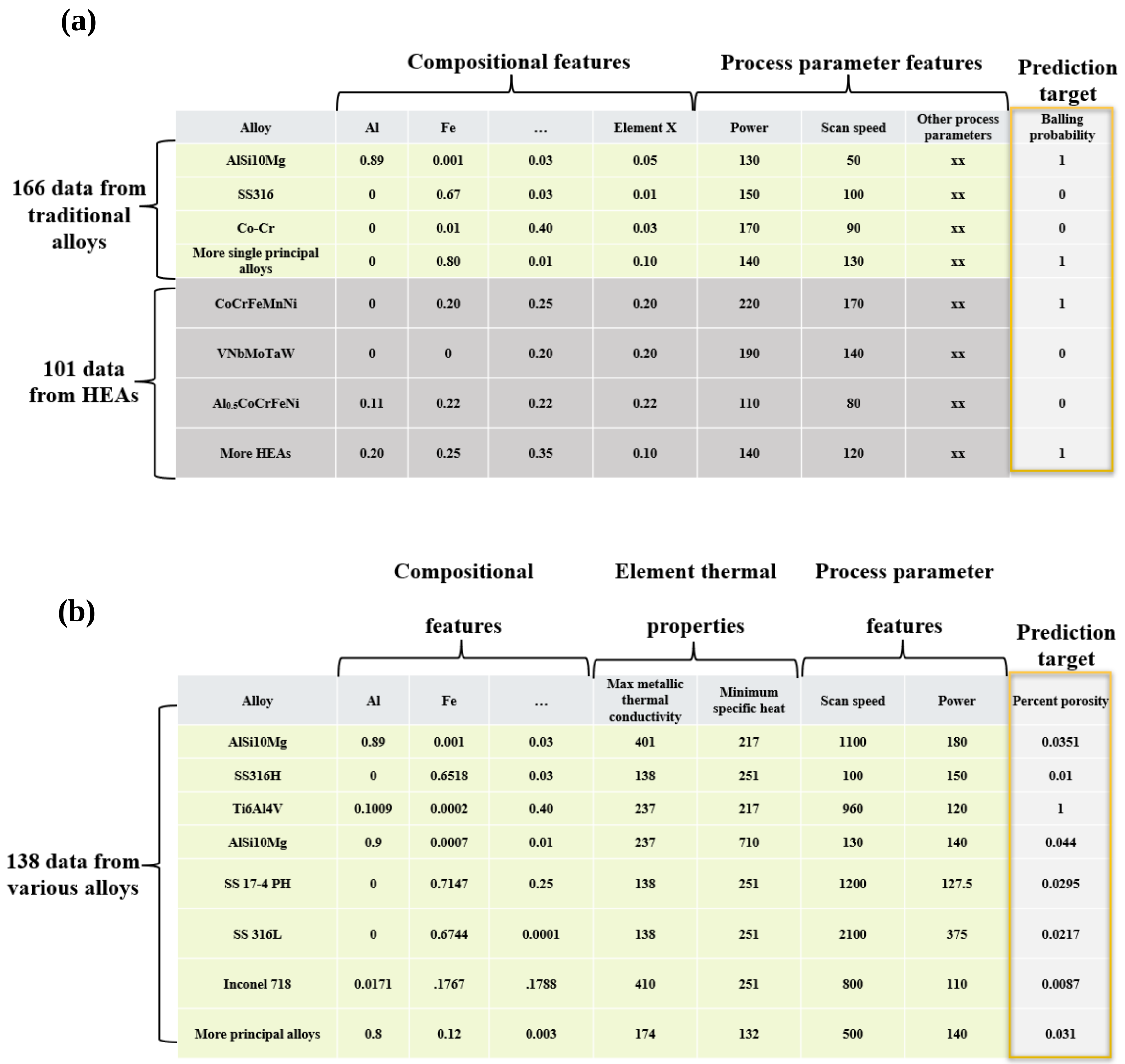

(a)

		Compositional features				Process parameter features			Prediction target
	Alloy	Al	Fe	…	Element X	Power	Scan speed	Other process parameters	Balling probability
166 data from traditional alloys	AlSi10Mg	0.89	0.001	0.03	0.05	130	50	xx	1
	SS316	0	0.67	0.03	0.01	150	100	xx	0
	Co-Cr	0	0.01	0.40	0.03	170	90	xx	0
	More single principal alloys	0	0.80	0.01	0.10	140	130	xx	1
101 data from HEAs	CoCrFeMnNi	0	0.20	0.25	0.20	220	170	xx	1
	VNbMoTaW	0	0	0.20	0.20	190	140	xx	0
	$Al_{0.5}CoCrFeNi$	0.11	0.22	0.22	0.22	110	80	xx	0
	More HEAs	0.20	0.25	0.35	0.10	140	120	xx	1

(b)

		Compositional features			Element thermal properties		Process parameter features		Prediction target
	Alloy	Al	Fe	…	Max metallic thermal conductivity	Minimum specific heat	Scan speed	Power	Percent porosity
138 data from various alloys	AlSi10Mg	0.89	0.001	0.03	401	217	1100	180	0.0351
	SS316H	0	0.6518	0.03	138	251	100	150	0.01
	Ti6Al4V	0.1009	0.0002	0.40	237	217	960	120	1
	AlSi10Mg	0.9	0.0007	0.01	237	710	130	140	0.044
	SS 17-4 PH	0	0.7147	0.25	138	251	1200	127.5	0.0295
	SS 316L	0	0.6744	0.0001	138	251	2100	375	0.0217
	Inconel 718	0.0171	.1767	.1788	410	251	800	110	0.0087
	More principal alloys	0.8	0.12	0.003	174	132	500	140	0.031

Figure 2. General overview of the datasets and descriptors used to predict (a) balling and (b) the porosity.

3.1.2 Elemental Properties List

An initial data analysis of the training dataset was carried out to identify the existing correlations between a random pair of the descriptors. The Pearson correlation coefficient is an accurate indicator of the correlation, where $P = +1$ (-1) indicates a strong positive (negative) correlation. A heatmap of all the correlations in Figure 3 shows that concentrations of oxygen, hydrogen, and nitrogen are positively correlated and so are the concentrations of lead and tin. Some strong correlation is also seen between the concentrations of aluminum and magnesium.

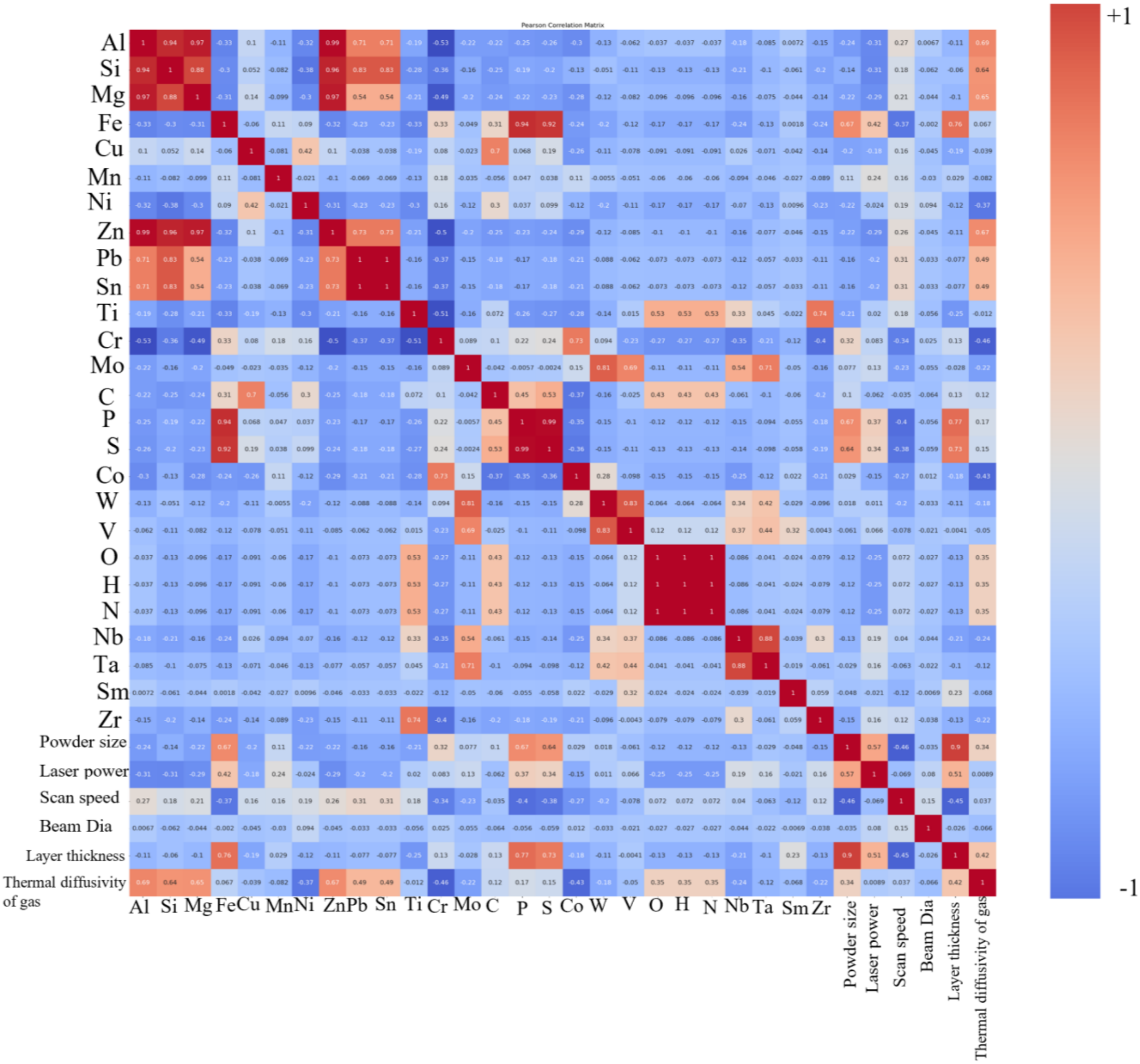

Figure 3. Heat map showing the Pearson correlation coefficients between all pairs of descriptors in the balling dataset.

In order to study the effect of the nature of dataset on the prediction accuracy, the balling dataset was divided into two sets:

1. Dataset 1 consisting of traditional alloys without the HEA data
2. Dataset 2 consisting of both traditional alloys and HEAs.

All three models were trained once on Dataset 1 and then on Dataset 2, and results from both datasets were obtained and compared.

3.2 ML Models

Gradient boost regressor: The GBR model (Friedman 2001) works by making an initial guess from the training data called the leaf, which is the prediction output for all data in the dataset. The model starts with a guessed value equal to the average of all the outputs in the training data. It then builds a network or tree such that every node in the network is a conditional loop based on the error (the difference between the observed and predicted outputs) encountered in the previous loop. The number of leaves in every tree is bound from 8 to 32. For every new tree that is built in progressive steps, the pseudoresiduals of all data are calculated and scaled by a parameter called the “learning rate” by simple multiplication; that becomes the contribution from that particular tree.

Random forest: The RF classifier (Breiman 2001) consists of a combination of decision tress working in tandem to individually predict the output of each data point; the overall prediction is then determined by a voting algorithm. This model balances the bias and variance well and has been used widely in other alloy studies where data are limited (Kaufmann and Vecchio 2020). The RFR model follows the same overall structure as the RF classifier. The decision trees vote for the position of the output of each data point; then, the overall votes are averaged to make the final prediction (Probst and Boulesteix 2017). The best predictions were found with n_estimators = 399.

Neural Network: Artificial NNs closely replicate the human brain’s neuron network in the form of a computer algorithm (Dayhoff 1990). They comprise several layers of nodes, the inner and outer layers being the first and last ones. Every node in a layer acts as a neuron that has a certain threshold for activation and an associated weight. The neuron is inactive below the threshold but transfers data to the next layer when the input exceeds the threshold. The optimized architecture of the NN in this work was set as 2 hidden layers with 16 and 8 nodes each. The activation function was set to a rectified linear unit (ReLU) (Fukushima 1975), and 1,000 epochs were used in training.

3.3 Results and Discussion

The performance of the three models is shown by the prediction accuracy in Table 3. The NN is the most accurate model of the three for the balling datasets, and the accuracy increases when both traditional alloys and HEAs are combined in the balling training set. The RFR is the most accurate model for the porosity data. The NN model performed below expectations with large errors in the predictions. It was not able to adequately predict any porosity value that was not within the common range of the dataset, i.e., 0.1%–0.2%. When presented test data that had a true value outside this range, the model instead predicted a value in line with the rest of its predictions. The model was also not differentiating between data points that had the same porosity and material but different processing parameters.

Table 3. Prediction accuracy of the three models using the two datasets.

Model	Accuracy with balling Dataset 1 (no HEAs) (%)	Accuracy with balling Dataset 2 (with HEAs) (%)	Porosity R^2 score	Mean squared error (MSE)	Root mean squared error (RMSE)	Mean absolute error (MAE)
RF Classifier	69.2	73.1	NA	NA	NA	NA
RF Regressor	NA	NA	0.971	0.0119	0.109	0.0518

GBR	84.6	88.5	0.955	0.0184	0.1357	0.0739
NN	88.5	92.3	0.0221	0.421	0.649	0.343

An important point to be noted is that the RF classifier used on the balling data is a classifier algorithm, and it only classifies either the occurrence (1) or absence (0) of balling, where 0 and 1 are the only discrete outputs from the RF classifier. However, the RFR, GBR, and NN are regression models, which means that during training, the outputs are learned as continuous variables. Thus, the predictions from the RFR, GBR, and NN can be any value between 0 and 1 as a probability of occurrence of balling rather than a discrete 0 or 1. This provides an opportunity to exploit the model for studying the impact of changing the elemental concentrations on balling defect formation by observing an increasing or decreasing trend in the probability. This style of modeling is required for predicting the porosity since the outputs are percentages, not classes or likelihood of belonging to the class.

Figure 4 presents the feature importance obtained from the Shapley additive explanations (SHAP) values. For the NN model trained on both datasets, it is seen that along with the process parameters (laser power and scan speed), some chemical features, like the Cu, Si, S, Fe, W, and Nb concentrations, seem to be significantly impacting the output. When the NN was trained on Dataset 1 (without the HEAs), the Cu, Si, C, S, and Fe concentrations are some of the most significant chemical descriptors. The connection to the laser power can be seen as sufficient melting of the powder, while high scan speeds mean the opposite, i.e., insufficient melting (Chen, Wei et al. 2017). When the NN was trained on Dataset 2, the C and S concentrations remain as some of the most significant features, but the W and Nb concentrations occupy the following ranks because of the inclusion of HEAs. Dataset 1 had around 40 data points with steel and 20 data points with Inconel 718 that were the major alloys containing carbon. Despite the differences in the nature of the training dataset, the C and S concentrations seem to be consistently impacting the occurrence of balling. If steel is considered as a test alloy, it is common knowledge that the carbon content heavily impacts the properties of steel including solidification (Wolf and Kurz 1981) and deformation and corrosion (Trillo and Murr 1998). The model uses the carbon concentration differently in the different datasets, as indicated by the change in sign of the SHAP value. For steel, it is related to an increase in balling, but in HEAs, it is tied to a decrease in balling. Our NN model interprets the carbon concentration as one of the significant descriptors to determine the occurrence of balling defects, thereby validating the model’s power to make meaningful and practical recommendations for the experimentalist.

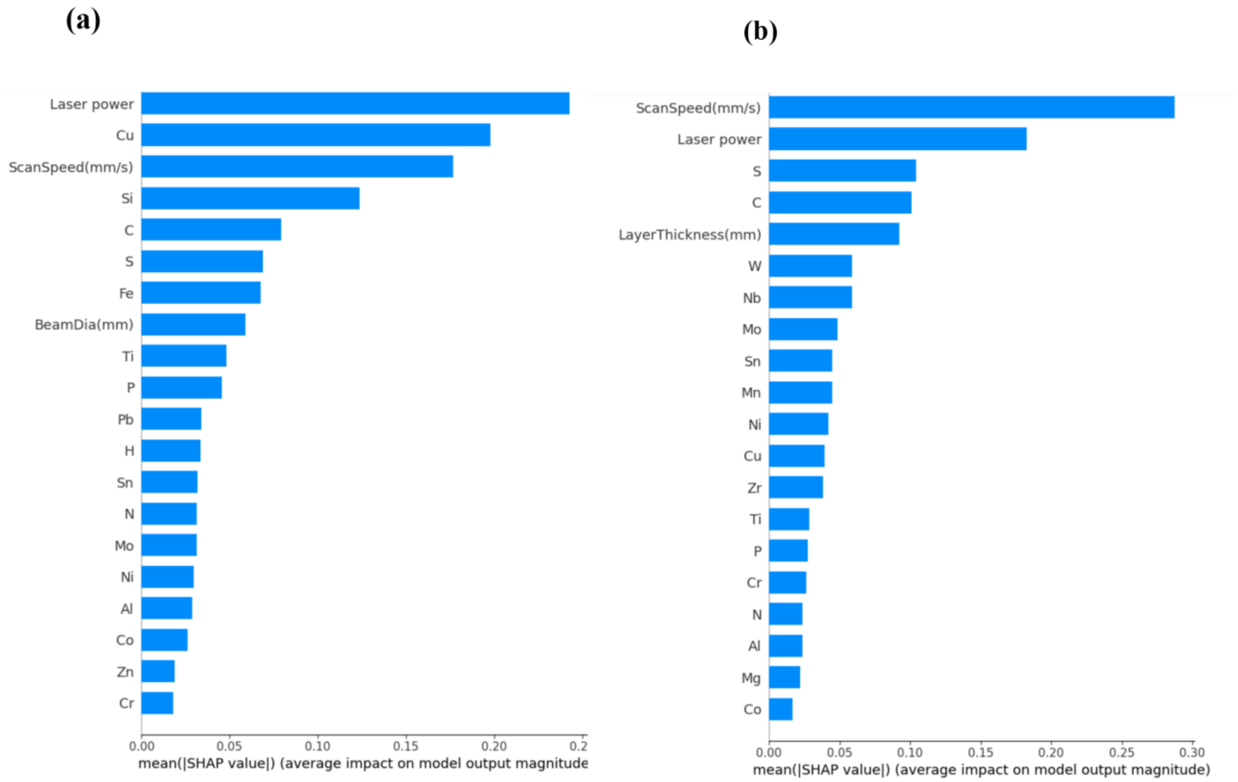

Figure 4. Feature importance ranked in decreasing order for the NN model trained on (a) Dataset 1 and (b) Dataset 2.

Overall, the most accurate model i.e., the NN model trained on Dataset 2 (including the HEAs) and the combined porosity model show a high accuracy of predictions and highlight the carbon concentration as an important variable in determining combined defect formation, which is in line with the metallurgical principles of the effects of carbon in steel.

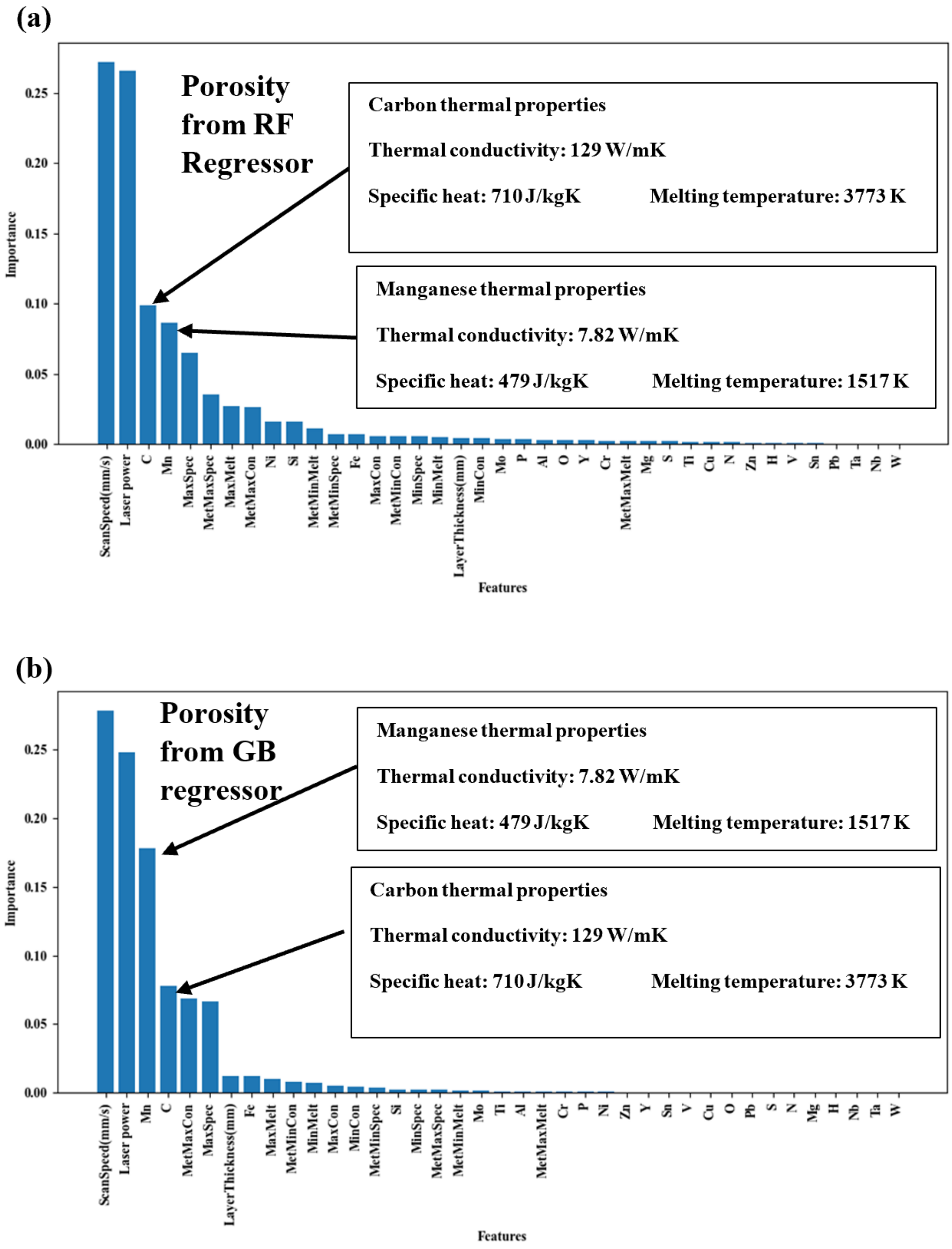

Figure 5. Model feature importance for porosity predictions: (a) RFR and (b) GBR.

While the overall accuracy of the models did not greatly change, the feature importance varies, as seen in Figure 5(a) and (b). The top two are to be expected because of the nature of LPBF manufacturing. The carbon and manganese concentrations are both important elemental descriptors for both models; however, the GBR model has placed much more importance on the manganese concentration than the RFR model. The manganese concentration and the maximum specific heat of the elements present are the strongest elemental descriptors shared by the models. The maximum specific heat of the elements present is a property of carbon for much of the dataset and is a moderate predictor in the model. The RFR has a more evenly distributed importance over the other features past layer power and scan speed. The carbon concentration is a top feature, with ~8% and ~10% for the GBR and RFR, respectively.

To systematically investigate the influence of the carbon concentration on the printability of stainless steels, a targeted system was selected for multiphysics simulations using FLOW-3D. These simulations were conducted through a collaborative effort between Pacific Northwest National Laboratory (PNNL) and Oregon State University (OSU), focusing on DED processes applied to SS316L and SS316H. Initial trial simulations were carried out utilizing the default material properties of SS304 as a benchmark, with representative results displayed in Figure 6.

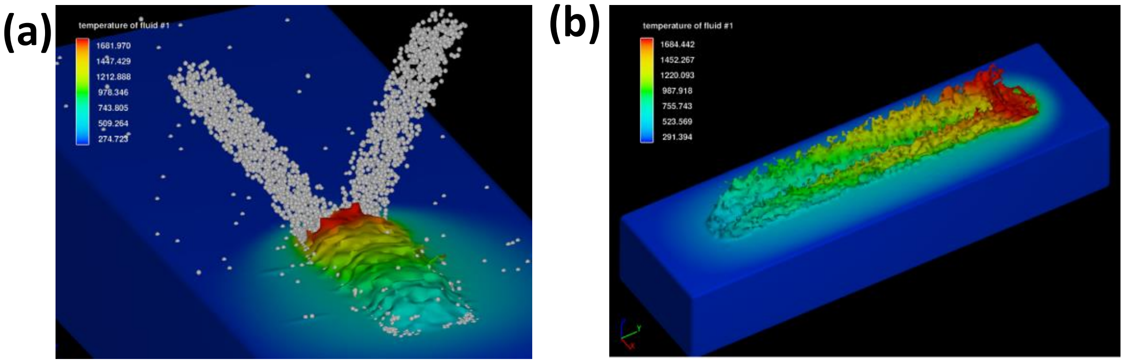

Power: 38 Watts
Laser Speed: 2 cm/s
Powder velocity: 39.4 cm/s

Power: 100 Watts
Laser Speed: 2 cm/s
Powder velocity: 39.4 cm/s

Figure 6. Initial trial simulations performed by OSU using the default SS304 material properties under varying power conditions: (a) 38 and (b) 100 W.

To refine the simulation model for SS316L and SS316H, it was imperative to incorporate precise temperature-dependent properties such as the thermal conductivity, specific heat capacity, density, viscosity, and surface tension, along with non-temperature-dependent properties like the liquidus and solidus temperatures and latent heat of fusion. These critical thermophysical properties for SS316L and SS316H were meticulously obtained through the Thermo-Calc software, leveraging PNNL’s licensed access to the database. Utilizing this enhanced material dataset, OSU initiated trial simulations by modifying an existing SS304 template within FLOW-3D to accommodate the specific properties of SS316L and SS316H. Preliminary results from these simulations are depicted in Figure 7.

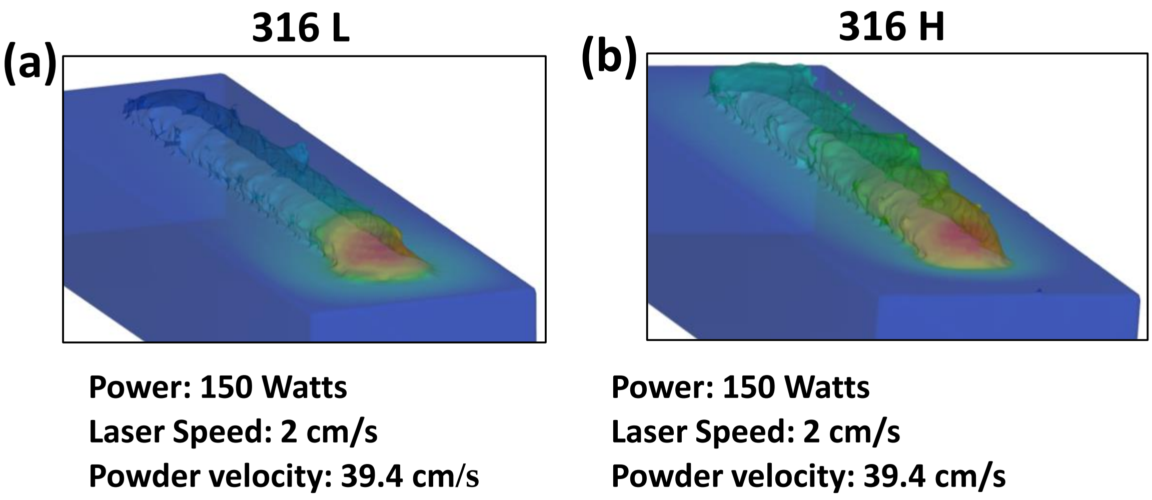

Figure 7. Results of trial simulations conducted by OSU utilizing the accurate material properties of (a) SS316L and (b) SS316H. The simulations were performed using identical process parameters for both materials, as indicated in the figure. A qualitative analysis of the printed tracks suggests that SS316L produced a more uniform and visually superior track compared to SS316H.

3.4 Summary

In summary, a chemical-composition-based ML model is proposed for predicting the tendency of balling defect formation and the porosity in alloys during AM using a laser-based method. The dataset was curated from the literature that included traditional alloys and HEAs, with a total of 267 data points describing balling defect formation under various processing conditions in these alloys and 138 data points describing the porosity for various processing parameters, along with element-specific properties. Three models—an RF classifier, a GBR, and an NN—were trained on two datasets (Dataset 1: excluded HEAs and Dataset 2: included HEAs), and their accuracies were calculated from the testing data. The NN model trained on Dataset 2 proved to be the most accurate in predicting balling defect formation with an accuracy of 92.3%. Two models—RFR and GBR—were trained on the porosity dataset. The RFR was the most effective at predicting the porosity with the lowest mean squared error (MSE) of 0.0119. These models revealed that along with the processing conditions such as laser power and scan speed, the silicon and carbon concentrations significantly influence the tendency to form balling defects, while the thermal conductivity and carbon concentration were significant factors in the porosity. The inclusion of steel data in the training set led to the identification of the carbon concentration as a significant contributor to both types of defects. These findings are in line with metallurgical principles, as it is known that small amounts of carbon can highly alter the solidification and deformation properties of steel, thus serving as initial validation of the models. In conclusion, the collaborative simulations conducted using ML and FLOW-3D have provided valuable insights into the impact of alloy composition, particularly the carbon concentration, on the printability of SS316L and SS316H during AM processes. The findings underscore the importance of tailored compositional adjustments in optimizing process outcomes and pave the way for further refinement of AM processes.

4.0 Laser Directed Energy Deposition

Laser-based AM of metals using powder feedstock can be accomplished via two widely used technologies: DED and LPBF. In general, metallic powder is delivered to a location (e.g., build plate) and locally melted with a laser heat source in both DED and LPBF. The material undergoes rapid cooling and solidification upon deposition, and with the addition of subsequent layers, the material within the component is subjected to rapid thermal cycles. Typically, the laser generates a melt pool on a substrate or previous material layer as more material is added to the melt pool. As the laser proceeds along the scanning direction, the melt pool cools and solidifies, fusing (joining) the material to the layer below. This is what is referred to as the layer-by-layer fashion, as the process is repeated to build a 3-D component. In DED, the powder can be delivered to a location on the build plate using a single/double nozzle and often results in deposition where desired. Upon completion of the job, the component needs to be extracted from the powder bed, which is generally surrounded by unmelted powder (Carroll 2015).

DED provides a balance between dimensional resolution and component fabrication speed and can create fully dense (i.e., >99 wt%) components. Additionally, DED can easily print different materials in the same machine, while LPBF requires significant efforts to switch from one material to another. This work focuses on optimizing the laser parameters of the DED process for A709, G91, and G92 alloys.

4.1 Process Parameter Optimization for DED

Past AM research has mostly focused on typical stainless-steel alloys such as grade type 304 and 316. With interest in the application of metal AM to next-generation nuclear reactors, this work encompasses a survey of process parameters in found in literature applicable to AM fabrication of three alloys: A709, G91, and G92.

The three alloys are listed in Table 4, along with the compositions of their powders to be used for DED. Powder particle sizes are in the range of 50–150 µm. The primary difference between G91 and G92 is that the latter has additional tungsten content of 1.9 wt%, which could embrittle the material. Both grades are F/M alloy steels, while Type A709 is an austenitic stainless steel with high Cr and Ni contents compared to 316L stainless steel. One reason that G91 and G92 are attractive for next-generation nuclear reactors is due to their lower and higher thermal expansion, respectively, than that of 300-series austenitic stainless steels (Abe 2014). Additionally, both F/M steels can be heat-treated to target a specific ratio of ferrite-to-martensite, enabling a wide range of mechanical properties. Meanwhile, the thermophysical properties of A709 are similar to other high Cr and Ni stainless steels (Smith, Lybeck et al. 2017), and A709 has good weldability, which is attractive for AM applications (Sham, Bass et al. 2022).

Table 4. Compositions (wt%) of the three steel alloy DED powders evaluated in the literature survey.

	B	C	Cr	Fe	Mn	Mo	N	Nb	Ni	Si	V	W
A709	0.009	0.04	20.6	Bal.	0	1.4	0.15	0.3	25	0.1	0	0
Grade 91	0	0.07	8.5	Bal.	0.4	0.94	0.06	0.07	0	0.3	0.19	0
Grade 92	0	0.09	8.8	Bal.	0.4	0.4	0.09	0.08	0	0	0.19	1.7

4.1.1 Laser Parameters for A709

The 300 series austenitic stainless steels, which have seen extensive research in relation to a multitude of AM processes, have similar microstructures, mechanical properties, and thermophysical properties to those of A709 steel (Smith, Lybeck et al. 2017), and the relevant publications with the associated process parameters are detailed in Table 5. Type A709 steel also has good weldability (Sham 2022), which bodes well for its fabrication using DED.

The elements Cr and Ni both play vital roles in determining the phase of a steel alloy and preventing or enabling alloy cracking and embrittlement (Bansod, Shukla et al. 2023). Cr_{eq} and Ni_{eq} in Equations (1) and (2), respectively, more explicitly combine Cr or Ni with other alloy elements to determine whether the alloy in question is susceptible to embrittlement or cracking (Hossein Nedjad, Yildiz and Saboori 2023).

$$\mathrm{Cr_{eq}} = \%\mathrm{Cr} + \%\mathrm{Mo} + 1.5 \times \%\mathrm{Si} + 0.5 \times \%\mathrm{Cb} + 5 \times \%\mathrm{V} + 3 \times \%\mathrm{Al} \tag{1}$$

$$\mathrm{Ni_{eq}} = \%\mathrm{Ni} + 30 \times \%\mathrm{C} + 0.87 \times \%\mathrm{Mn} + 0.33 \times \%\mathrm{Cu} + (\%\mathrm{N} - 0.045) \tag{2}$$

Combining Table 4 with Equations (1) and (2) results in Cr_{eq} = **22.81** and Ni_{eq} = **28.83** for Cr_{eq}/Ni_{eq} = **0.79**. From Figure 8(a) below, Cr_{eq}/Ni_{eq} = **0.79** creates a primary austenite with no ferrite phase microstructure, similar to 316L stainless steel with certain DED process parameters (Marya, Singh et al. 2015). When fabricated using DED, an austenitic stainless steel with Cr_{eq} and Ni_{eq} contents as high as those in Type A709 steel may be susceptible to hot cracking, as shown in the modified Bystram diagram (Hossein Nedjad, Yildiz and Saboori 2023) in Figure 8(b). However, Ni_{eq} is higher than the range of *y*-axis values of the plot, and at a combination of both high Cr_{eq} and high Ni_{eq}, hot cracking susceptibility may be diminished. Note that the equations in Figure 8(a) for Cr_{eq} and Ni_{eq} are slightly different from Equations (1) and (2) but result in nearly identical values of Cr_{eq} = 22.81 and Ni_{eq} = 28.36 for Cr_{eq}/Ni_{eq} = **0.80**.

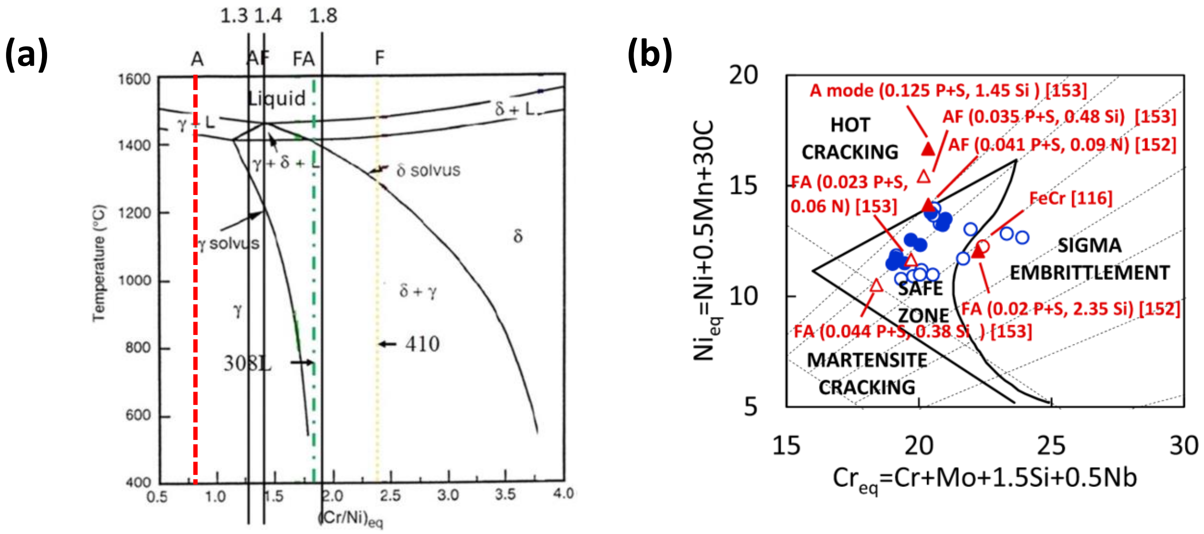

Figure 8. (a) Fe–Ni–Cr pseudo-binary phase diagram (Bansod, Shukla et al. 2023), (b) DED stainless steels on a modified Bystram diagram (Hossein Nedjad, Yildiz and Saboori 2023).

Because of the potential for hot cracking susceptibility of Type A709 steel, special consideration should be made for its process parameters. Using a lower laser power than compared to the wide range of laser powers for 300-series steels in Table 5 will reduce the thermal gradient and cooling rate, which in turn decreases the risk of hot cracking during DED fabrication through increased uniformity in cooling and solidification of the specimens. Meanwhile, decreasing the scan speed relative to the range of values in Table 5 also decreases the hot cracking susceptibility through more uniform solidifcation.

Table 5. Literature on DED process parameters for austenitic stainless steels.

Machine	Alloy	Laser Power, W	Laser Scan Speed, mm/s	Hatch Spacing, mm	Powder Mass Flow Rate (PMFR), g/min	Layer Thickness, mm	Laser Spot Size, mm	Porosity, %	Ref.
Optomec LENS 750	304L	400	17	0.41	16	0.25	-	<0.5	(Smith, Sugar et al. 2018)
Trumpf TruLaser Cell 7040	316L	1600	13.3	2	10	0.4	2	0.05–0.3	(Feenstra, Cruz et al. 2020)
ROFIN CO$_2$ laser	316L	1,400–5,000	5–28	-	9.8–37.5	0.5	0.5–1.8	2.5–3.5	(Ma, Wang et al. 2013, Ma, Wang and Zeng 2016)
Diode laser	316L	1,400	16.7	-	14	-	3	0.09–0.20	(Zhi'En, Pang et al. 2018)
Optomec LENS® 3D Hybrid 20	316L	250/475/700	3.3/6.7/10	-	10/20/30	0.71-6.9	0.5	0.5–12	(Amar, Popov et al. 2023)
Optomec LENS MR7	316	100/200/250	8.5/12.7/17	0.381	7/10/13.5	0.254	-	0.5–18	(Izadi, Farzaneh et al. 2017)
POM-DMD 105D	316L	400/600/800	5/8.3/11.7	-	2/3/4	-	-	-	(M and Senthilkumar 2021)
LDF 6000-100 diode laser	316L	2,000	8.3	3	-	1	5	-	(Guo, Zou et al. 2017)
750 W CW Fiber Laser, Wuhan Raycus Fiber Laser Technologies	316L	400/700	2/10	-	10/30	-	3	-	(Kim, Kang and Lee 2019)
CW Yb fiber laser (IPG Photonics)	316L	250/328/270–516	16.9	0.25	28	0.38	-	0.5–21.5	(Zheng, Haley et al. 2019)
IPG 2000 fibre laser	316L	1,000	6/8/10/12	1	-	0.5	-	0.7–6.9	(Yang, Gong et al. 2020)
AMBIT, Hybrid Manufacturing Technologies	316	600/700/800/900/1,000	8/9/10/11/12	-	5	0.54	2	-	(Era and Liu 2021)
TRUMPF 6-kW TruDisk 6002	316L	1,200/1,400/ 1,600/1,8	5/6/7/9/11	-	10.7/13.2/15.1/17.6/20.8/22.6	Varied	3	0.09–0.33	(Lin, Shen et al. 2020)

Yb:YAG disk laser		00/ 2,000							
Optomec LENS 850M	316L	645	2.1–19	-	3.34–8.6	-	-	1.1	(Sciammarella and Salehi Najafabadi 2018)
Optomec LENS 750	316L	360	16.3	0.39	10	0.25	-	-	(Yang, Yee et al. 2016)
Optomec LENS 750	316L	360	8.5	0.5(/7.2?)	5.4	0.5	-	2.6–3.4	(Yadollahi, Shamsaei et al. 2015), (Yadollahi, Shamsaei et al. 2016)
ABB Robotics IRB 4600 + 3 kW fiber laser	316L	900	15	-	-	-	-	-	(Saboori, Piscopo et al. 2020)
2 kW continuous wave fiber laser	316	1,000/1,200/ 1,400	6.7/8.3/10	-	3/6/8	-	3.2	-	(Benarji, Kumar et al. 2020)
Optomec LENS MR7	316L	400	15	0.45	-	0.3	-	-	(Ziętala, Durejko et al. 2016)
Laserline model LDF 4000-100	316L	1,000	6	-	4.68	0.1–0.2	-	-	(Wang, Palmer and Beese 2016), (Bronkhorst, Mayeur et al. 2019)
Optomec LENS MR7	316L	380	-	0.46	6.3	0.3	-	-	(Bronkhorst, Mayeur et al. 2019)
YLR-500-MM-AC-Y14, IPG Photonics	316L	34.3/45.2	0.4/0.5/0.6	-	2.46/2.81/3.09	-	0.3	-	(Weng, Gao et al. 2019)
Optomec LENS 750	316L	200/375	2.3/4/25.4	0.3	10	0.1	-	-	(Hwa, Kumai et al. 2021)
InssTek MX600 3D	316L	417	14.2	-	180	0.25	0.8	-	(Azinpour, Darabi et al. 2020)
DMG Mori LASERTEC 65 3D	316L/TiB$_2$	1,000/1,200/ 1,400	3.3/6.7/10	-	5.44/7.85/9.95	1	3		(Ang, Sing and Lim 2022)
Irepa Laser Cladding (LC) system	316L/ WC	570	4.8	-	23.4	-	1.5	-	(Fetni, Enrici et al. 2021)
(Laserline Gmbh, LDM 1000–40	316L/Inconel 718	250–900	0.8	-	4	1.2	-	-	(Li, Kishore et al. 2023)
IREPA Laser	316	200/350	3.3/8.3	-	1.7	0.26/0.40/ 0.44	0.46	9	(de Lima and Sankaré 2014)
7 kW IPG fiber laser	316L	570/750	12.5/16.7	-	2/2.7	0.5	1.2	0.4	(Yu, Rombouts and Maes 2013)

IPG Photonics YLR-12000-L	304L	2,300/4,000	8.5/10.6	2.5	18/23	0.8/1.2	4		(Wang, Palmer and Beese 2016)

4.1.2 Laser Parameters for Grade 91 and Grade 92

AM of Grade 91 and Grade 92 F/M stainless steels has mainly utilized LPBF in past research. The limited publications on DED of F/M steels and the associated process parameters are outlined in Table 6. While no work has been found on DED of G92 steel, G91 is expected to be nearly identical in both performance and fabrication (Lienert and Maloy 2017). As such, it was determined that identical DED process parameters would be used for both G91 and G92 steels.

Of primary concern in the realm of F/M steels is the martensite start (M_s) temperature, which is controlled primarily by the Mn content, along with the Cr, Mo, Si, and C contents, where increased contents of these elements can decrease the M_s temperature. A high M_s temperature increases tensile residual stresses, which in turn increases the brittleness of the alloy (Zhong, Sridharan et al. 2021). Brittleness is of great concern during fabrication with DED processes due to the large thermal gradients and rapid cooling and solidification during fabrication. An aspect of the methodology for process parameter selection was a qualitative comparison of the above elements to determine whether M_s was improved compared to the relevant publications. Compared to Fe–9Cr (Whitt, Seede et al. 2023) and Fe–9Cr–2W–V (Gräning and Sridharan 2022), G91 and G92 steels have higher contents of most of the elements that lower the M_s temperature, and as such, the two latter alloys are likely less brittle than the two former alloys for the same process parameters. The other alloys in Table 6 have similar or identical compositions to those of the G91 and G92 steels, and all papers reported success with the selected process parameters. The process parameters for this work were selected from the ranges of values in Table 6.

Table 6. Literature on DED process parameters for F/M steels.

Machine	**Alloy**	**Laser Power, W**	**Laser Scan Speed, mm/s**	**Hatch Spacing, mm**	**Powder Mass Flow Rate (PMFR), g/min**	**Layer Thickness, mm**	**Laser Spot Size, mm**	**Porosity, %**	**Ref.**
DMD 103D system	ANA2	600	10	0.6	6	0.6	1.5	-	(Zhong, Sridharan et al. 2021, Tan, Zhong et al. 2022)
2 kW continuous fiber laser	Reduced activation steel	800	6	-	8	0.5	3	-	(Xia, Xu et al. 2020)
Optomec LENS 850R	Grade 91	400	5	-	2	0.2	1.4	-	(Villaret, Boulnat et al. 2021)
Optomec LENS 500	Fe–9Cr	260/320/380	3/5/7/9/11	0.35–0.71	3.3/6.24/9.3	0.22–1.97	0.7	0.04–13.35	(Whitt, Seede et al. 2023)
Optomec LENS MR7	Grade 91	-	-	-	-	-	-	-	(Samuha, Bickel et al. 2023)

Optomec LENS MR7	AF9628	200/250/300/350/400	4.23/6.35/8.47	0.31–0.87	4.7/6.4/8.2	0.11–0.44	0.6	0.05–0.83	(Vaughan, Elverud et al. 2023)
Modulo 450 by BeAM	Fe–9Cr–2W–V	700	11.7	0.6	6	0.5–0.6		-	(Gräning and Sridharan 2022)
DMD 103D System	HT9	-	-	-	-	0.6–0.8	1.5	-	(Sridharan, Gussev and Field 2019)

Based on the literature data and discussion in this section, it was determined that the optimal process parameter overlapped for the three alloys. The average laser powers and scan speeds in Table 6 related to G91 and G92 steels correlate with the low laser powers and scan speeds in Table 5 related to Type A709 steel. As such, a single range of process parameters was selected for use with all three alloys. The selected experimental envelope is presented in Table 7.

Table 7. DED process parameter matrix to be used for all three alloys.

Laser Power, W	Laser Scan Speed, mm/min
400, 500, 600, 700	500, 600, 700, 800

5.0 Characterization of Selected Alloys

In this study, three steels that have the potential for application in nuclear reactors were fabricated via a DED AM technique. Then, the AM-fabricated parts were characterized. The details of the characterization techniques utilized are provided in Table 8.

Table 8. Summary of materials characterization techniques utilized in this study.

Alloy Studied	OM	Surface Roughness	SEM	EBSD	XRD	Vickers Hardness
A709	✓	✓	✓	✓	✓	✓
Grade 91	✓	✓	✓	✓	✓	✓
Grade 92	✓	✓	✓	✓	✓	✓

EBSD: electron backscatter diffraction; OM: optical microscope; SEM: scanning electron microscope; XRD: X-ray diffraction

5.1 Characterization Techniques

5.1.1 Metallurgical Preparation and Optical Microscopy

In preparation for optical microscopy, the A709, G91, and G92 alloy samples were sectioned into XZ cross sections. Each sectioned sample was mounted in epoxy and prepared metallographically with grinding and polishing. All samples were given a final polish using 1 µm diamond polishing paste and a colloidal silica (0.05 µm) polishing suspension. Once the final polishing was completed, samples were examined using Olympus DSX510 metallurgical microscope.

5.1.2 X-Ray Diffraction Investigation

A D6 Phaser (Bruker Inc.) diffractometer was used to collect X-ray diffraction (XRD) patterns of the samples. The samples were mounted in epoxy, resulting a considerably high background, especially at low angles. The D6 Phaser is equipped with a theta/theta goniometer with a radius of 166.5 mm, Cu Kα radiation, and a 1.2 kW X-ray power generator. All XRD patterns were collected using 0.01° 2θ step size at 0.32 s per step over a 2θ range of 10°–120°. Each scan took ~1 h to complete.

5.1.3 Scanning Electron Microscopy and Electron Backscatter Diffraction Examination

An FEI Helios 660 Nanolab dual-beam focused ion beam (FIB) scanning electron microscope (SEM) was used to examine the cross-sectional phase constituents and microstructures of the A709, G91, and G92 samples. Primarily, the backscattered electron (BSE) imaging mode was utilized. Grain orientation mapping was performed by electron backscatter diffraction (EBSD) varying the step size from 0.2–0.5 µm using the Aztec Crystal software from Oxford Instruments.

5.1.4 Mechanical Properties via Vickers Hardness Tests

Vickers microhardness measurements were performed using a Sun-Tec (model: CM-802 AT) microhardness tester, operated with the ARS20 software for automated measurements. A load force of 300 gram-force was applied for a duration of 10 s for each indentation. A minimum array of 5 × 5 indentations was performed on each sample, each indentation separated by 0.5 mm. This spacing ensures that measurements were not influenced by neighboring indentations, providing reliable and repeatable hardness values. Calibration checks were conducted using Sun-Tec calibration standards (249HV0.3 and 297HV0.3) to verify that the instrument was calibrated. These checks confirmed that the hardness values measured were within ±2% of the calibration standard, ensuring the accuracy of the measurements.

5.2 Additive Manufacturing of Selected Alloys via DED

Commercial A709, G91, and G92 steel powders were acquired from Linde Advanced Material Technologies Inc. (Indianapolis, IN). The nominal chemical compositions of the powders are presented in Table 4.

5.2.1 AM of Austenitic A709 Steel

Cubes with dimensions of 10 × 10 × 10 mm^3 were fabricated with various laser powers (400–800 W), scan speeds (600–900 mm/min), and hatch spacings (0.45, 0.9 mm) to optimize the A709 alloy build quality that results in a fully dense structure. The powder feed rate was fixed at 1 rpm. Additionally, two samples with same thickness (0.53 mm) were deposited with laser power of 400W and 800W and same scan speed (600 mm/min) for all three alloys. These depositions were done to understand the effect of layer thickness setting on deposition characteristics in DED process of this alloy. In DED process, depositing the layers in a fixed-thickness fashion does not usually ensure the accuracy of the part geometry because the heights of the deposited layers vary depending on the laser power and scan speeds. Hence, a study on constant thickness setting procedure is proposed that allows the slice thickness to be adapted as a function of both the actual deposited height and the process conditions. The examination of these specimen for surface finish and build quality will be carried out in next FY work. Table 9 presents the AM processing parameters employed to fabricate the A709 samples.

Table 9. AM processing parameters employed to fabricate the A709 samples.

Sample	Power (W)	Scan Speed (mm/min)	Feed Rate (rpm)	Hatch Spacing (mm)
1	400	600	1	0.9
2	400	700	1	0.9
3	400	800	1	0.9
4	400	900	1	0.9
5	500	600	1	0.9
6	500	700	1	0.9
7	500	800	1	0.9
8	500	900	1	0.9
9	600	600	1	0.9

Sample	Power (W)	Scan Speed (mm/min)	Feed Rate (rpm)	Hatch Spacing (mm)
10	600	700	1	0.9
11	600	800	1	0.9
12	600	900	1	0.9
13	700	600	1	0.9
14	700	700	1	0.9
15	700	800	1	0.9
16	700	900	1	0.9
17	800	600	1	0.9
18	800	700	1	0.9
19	800	800	1	0.9
20	800	900	1	0.9
21	400	600	1	0.9 (constant height 0.53 mm)
22	800	600	1	0.9 (constant height 0.53 mm)
23	450	500	1	0.9
24	350	500	1	0.45
25	400	500	1	0.45
26	500	500	1	0.45

5.2.2 AM of F/M Grade 91 and Grade 92 Steels

Cubes with dimensions of 10 × 10 × 10 mm^3 were fabricated with various laser powers (400–800 W), scan speeds (600–900 mm/min), and hatch spacings (0.45, 0.9 mm) for F/M (G91 and G92) samples to optimize the build quality that results in a fully dense structure. The powder feed rate was fixed at 1 rpm. This parametric study helped us to identify the processing window for the G91 and G92 steels, and tensile samples were fabricated with the optimized parameters. G91 tensile samples were fabricated using a laser power of 500 W, a scan speed of 600 mm/min, and a hatch spacing of 0.9 mm. G92 tensile samples were fabricated using a laser power of 500 W, a scan speed of 700 mm/min, and a hatch spacing of 0.9 mm. Table 10 and Table 11 present the AM processing parameters employed to fabricate the G91 and G92 samples, respectively. Macrophotographs of all AM fabricated samples are presented in Figure 9.

Table 10. AM processing parameters employed to fabricate the Grade 91 samples.

Sample	Power (W)	Scan Speed (mm/min)	Feed Rate (RPM)	Hatch Spacing (mm)
1	400	500	1	0.9
2	400	600	1	0.9
3	400	700	1	0.9
4	400	800	1	0.9
5	500	500	1	0.9

Sample	Power (W)	Scan Speed (mm/min)	Feed Rate (RPM)	Hatch Spacing (mm)
6	500	600	1	0.9
7	500	700	1	0.9
8	500	800	1	0.9
9	600	500	1	0.9
10	600	600	1	0.9
11	600	700	1	0.9
12	600	800	1	0.9
13	700	500	1	0.9
14	700	600	1	0.9
15	700	700	1	0.9
16	700	800	1	0.9
17	800	500	1	0.9
18	800	600	1	0.9
19	800	700	1	0.9
20	800	800	1	0.9
21	400	500	1	0.9 (constant height 0.63 mm)
22	800	500	1	0.9 (constant height 0.63 mm)
23	450	500	1	0.9
24	350	500	1	0.45
25	400	500	1	0.45
26	500	500	1	0.45

Table 11. AM processing parameters employed to fabricate the Grade 92 samples.

Sample	Power (W)	Scan Speed (mm/min)	Feed Rate (RPM)	Hatch Spacing (mm)
1	400	500	1	0.9
2	400	600	1	0.9
3	400	700	1	0.9
4	400	800	1	0.9
5	500	500	1	0.9
6	500	600	1	0.9
7	500	700	1	0.9
8	500	800	1	0.9
9	600	500	1	0.9
10	600	600	1	0.9
11	600	700	1	0.9

Sample	Power (W)	Scan Speed (mm/min)	Feed Rate (RPM)	Hatch Spacing (mm)
12	600	800	1	0.9
13	700	500	1	0.9
14	700	600	1	0.9
15	700	700	1	0.9
16	700	800	1	0.9
17	800	500	1	0.9
18	800	600	1	0.9
19	800	700	1	0.9
20	800	800	1	0.9
21	400	500	1	0.9 (constant height 0.69 mm)
22	800	500	1	0.9 (constant height 0.69 mm)
23	400	500	1	0.45
24	500	500	1	0.45
25	350	500	1	0.45
26	450	500	1	0.9

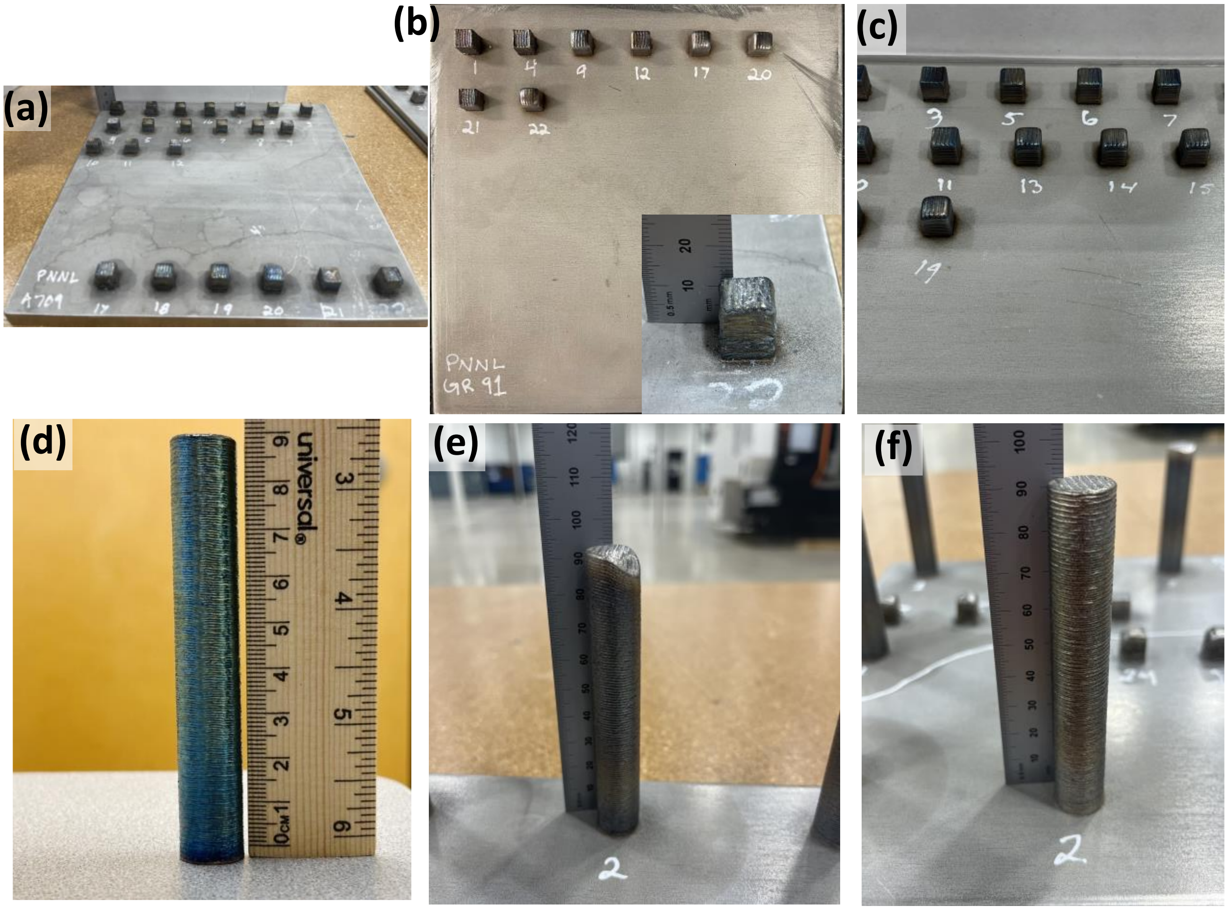

Figure 9. Fabricated cubes of (a) A709, (b) Grade 91, and (c) Grade 92 steels and tensile samples of (d) A709, (e) Grade 91, and (f) Grade 92 steels.

5.3 Characterization of Austenitic A709 Steel

5.3.1 Microstructural Analysis

Optical micrographs of A709 samples produced with various laser powers and scan speeds are presented in Figure 10. The samples had porosities of 0.03%–1.1%; however, cracks were observed in some samples. It was observed that a lower laser power produced denser products. Hence, tensile samples were fabricated with a laser power of 400 W and a scan speed of 600 mm/min, which was observed to be fully dense (99.97%).

Figure 11 presents representative backscattered electron micrographs of austenitic A709 steel (laser power: 400 W, scan speed: 600 mm/min) at different magnifications. The microstructure primarily consists of elongated grains with a cellular dendritic structure decorated within the grains. Representative EBSD orientation maps of austenitic A709 steel are presented in Figure 12.

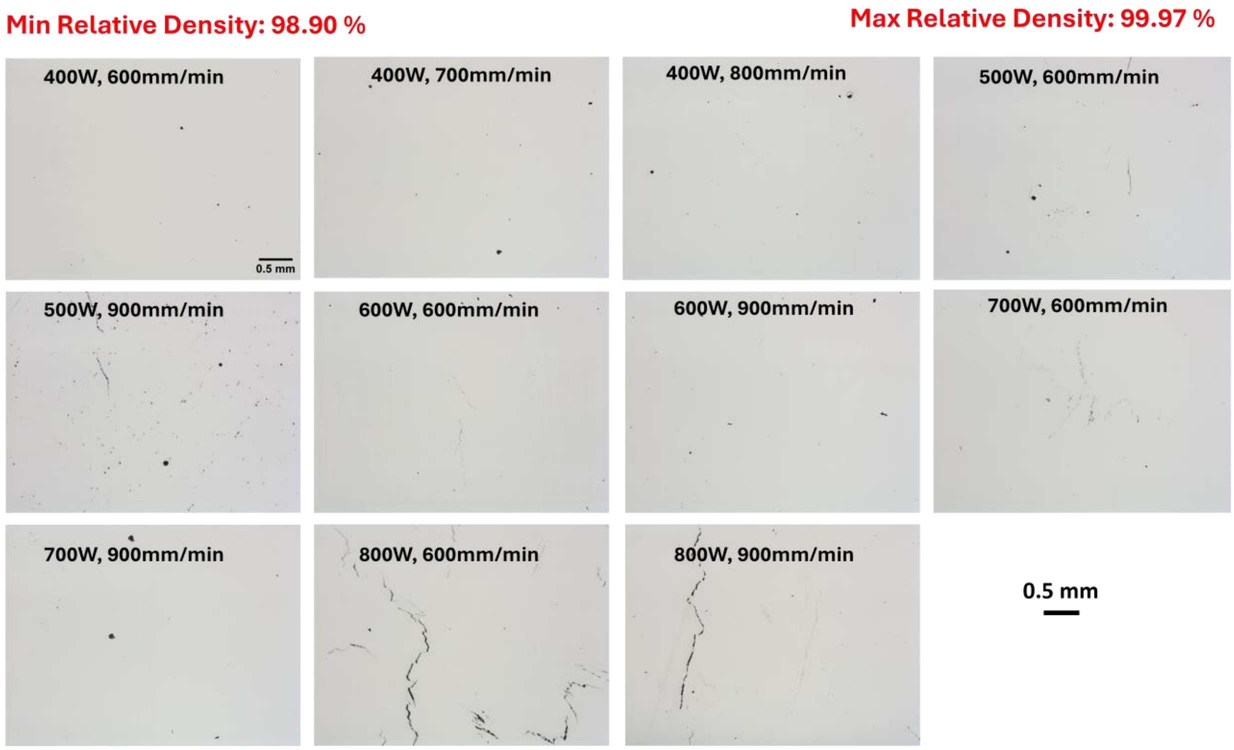

Figure 10. Optical micrographs of the XZ cross sections of A709 samples produced with various laser powers and scan speeds.

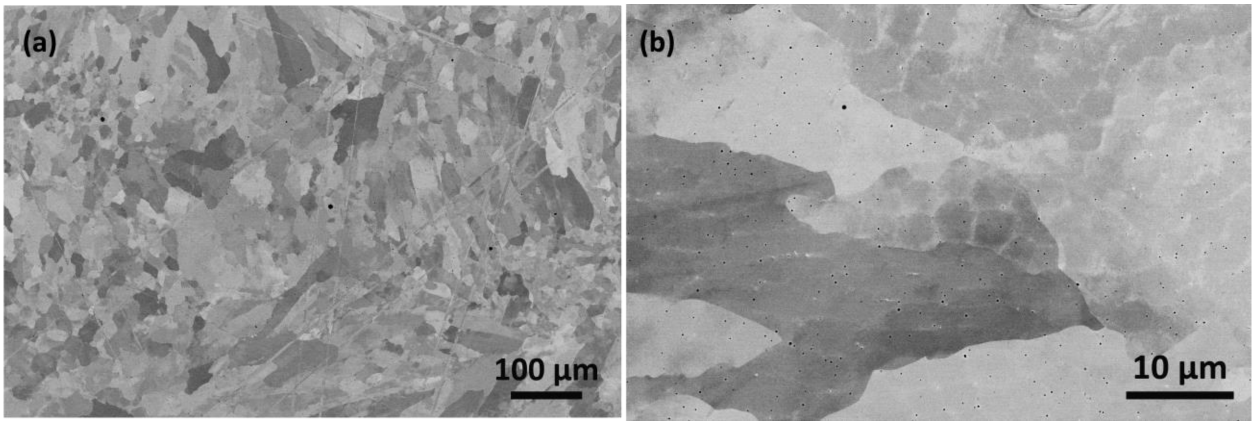

Figure 11. Representative backscattered electron micrographs of austenitic A709 steel: (a) low magnification and (b) high magnification depicting the dendritic cellular structure.

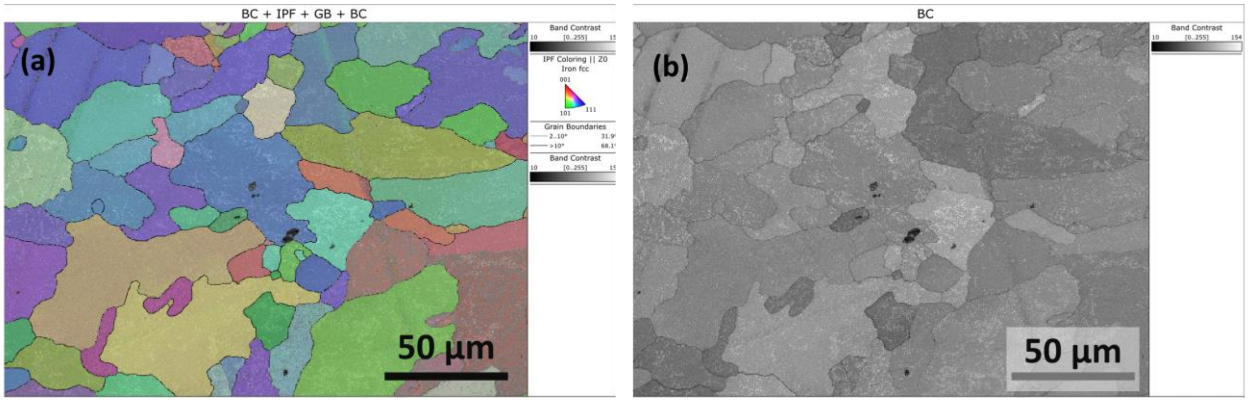

Figure 12. Representative EBSD orientation maps of austenitic A709 steel: (a) inverse pole figure and grain boundary contrast and (b) band contrast.

5.3.2 X-Ray Diffraction Analysis

Figure 13 presents a representative XRD pattern collected from an A709 sample. The main peaks identified were from the austenitic face-centered cubic (FCC) phase. Note that the signal coming from K_{beta} energy was not filtered out while this scan was performed; hence, low intensity repetitive peaks correspond to the same FCC phase were observed. Future scans would be performed with the X-ray diffractometer conditions that would filter out the K_{beta} signal.

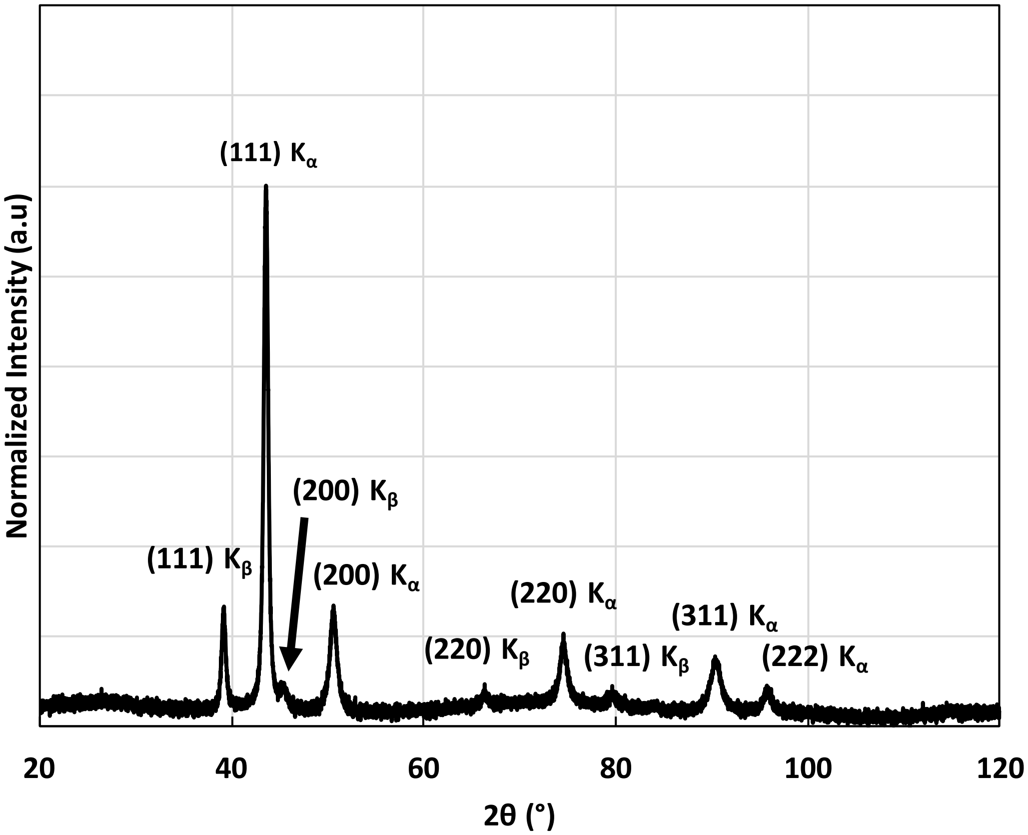

Figure 13. Representative XRD pattern of austenitic A709 steel.

5.3.3 Mechanical Properties of A709 Steel via the Vickers Hardness

The Vickers hardness of multiple samples of A709 steel was measured to understand the variation in hardness with the processing parameters. The average Vickers hardness collected from the A709 steel samples with various laser powers and scan speeds is presented in Table 12.

Table 12. Average Vickers hardness of austenitic A709 steel.

Laser Power (W)	Scan Speed (mm/min)	Vickers Hardness, HV
400	600	219.27 ± 7.79
400	700	212.77 ± 9.22
500	600	204.05 ± 8.25
600	600	198.79 ± 6.93
700	600	180.83 ± 8.22
800	600	171.63 ± 8.87

Figure 14 presents the variation in the Vickers hardness with the change in the laser power while the laser scan speed was kept constant. It was observed that in general, the Vickers hardness tended to decrease as the laser power increased when the laser scan speed was kept constant. This could potentially be attributed to the increase in grain size due to the higher laser power input.

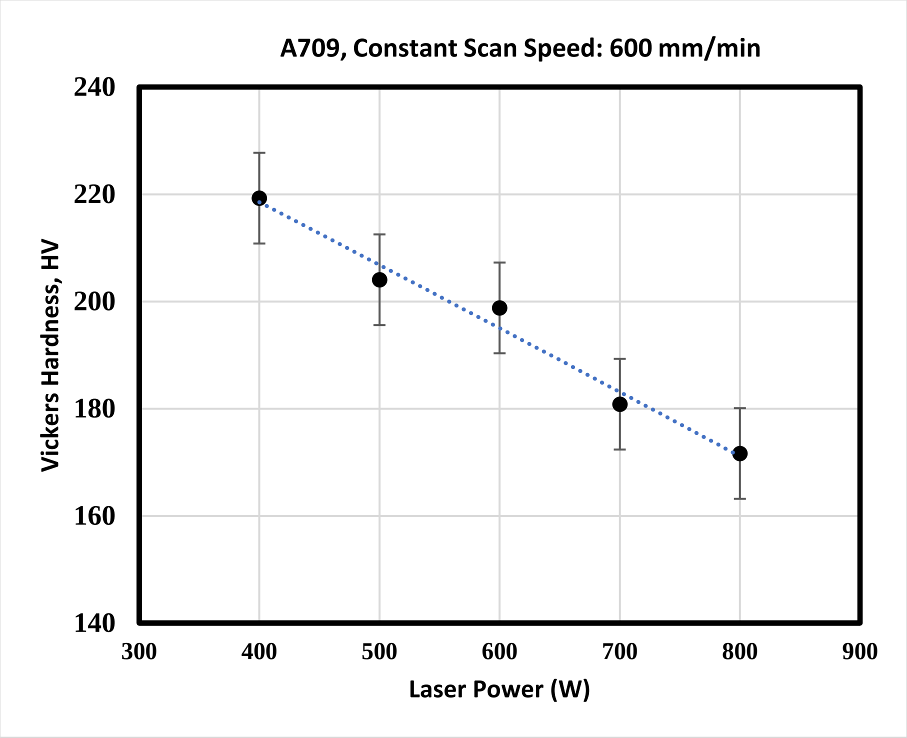

Figure 14. Variation in the Vickers hardness with the laser power at a constant scan speed for A709 steel.

5.4 Characterization of F/M Grade 91 and 92 Steels

5.4.1 Microstructural Analysis of Grade 91 Steel

Stitched optical micrographs of the XZ cross sections of the G91 samples produced with various laser powers and laser scan speeds are presented in Figure 15, allowing us to investigate the entire cross section. Some samples had a significantly higher number of pores, while few pores were also observed in some samples depending on the processing parameters, suggesting the importance of optimizing processing parameters to obtain a fully dense part. The relative densities of all the samples were determined, and porosity was observed to be 0.03%–3.62%. It was observed that a higher laser power yielded products with less porosity, so a laser power of 800 W and a scan speed of 500 mm/min were used to fabricate tensile bars [Figure 9(e)].

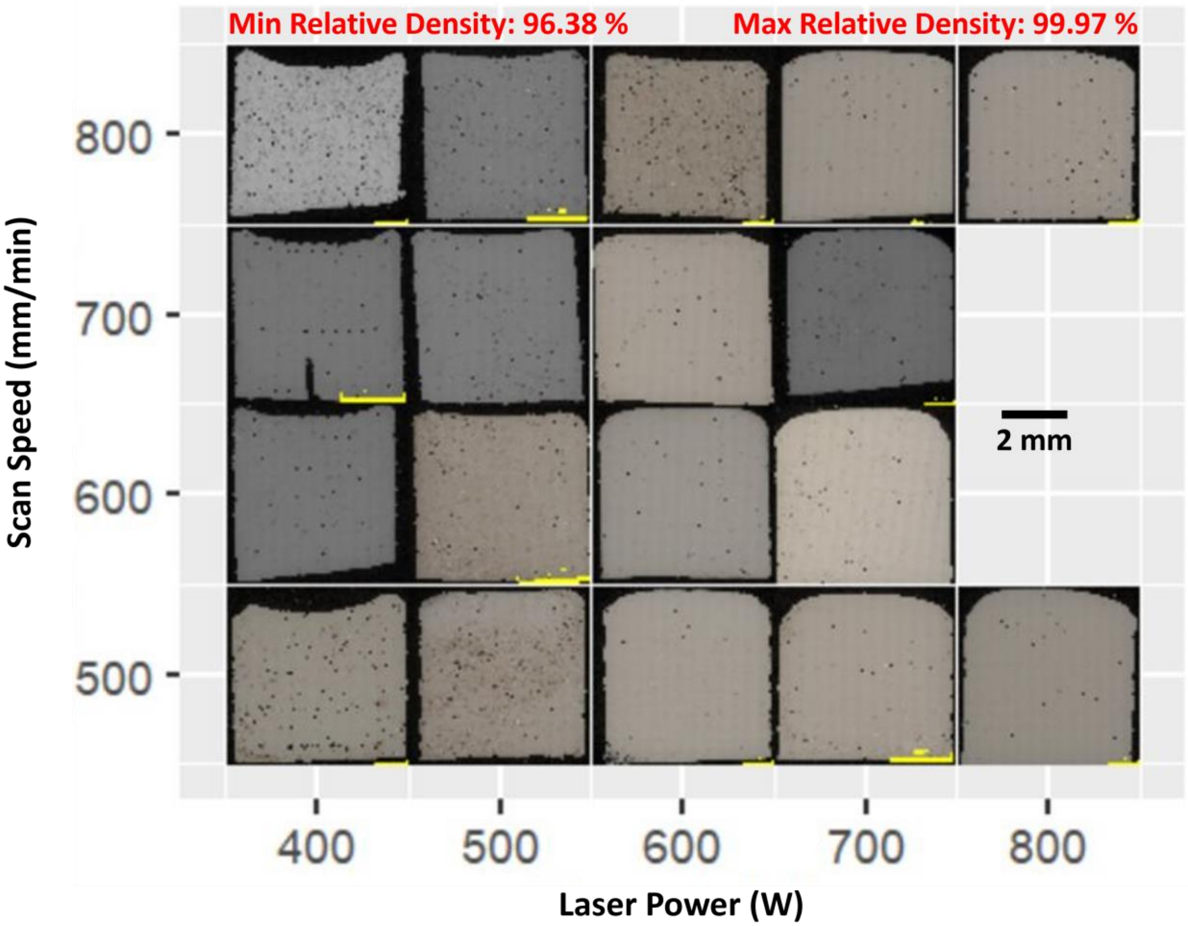

Figure 15. Stitched optical micrographs of the XZ cross sections of Grade 91 samples produced with various laser powers and laser scan speeds.

Figure 16 shows representative backscattered electron micrographs of F/M G91 steel (laser power: 800 W, scan speed: 500 mm/min) at different magnifications. The microstructure primarily consists of fine and coarsened lath martensite. Representative EBSD orientation maps of F/M G91 steel are presented in Figure 17.

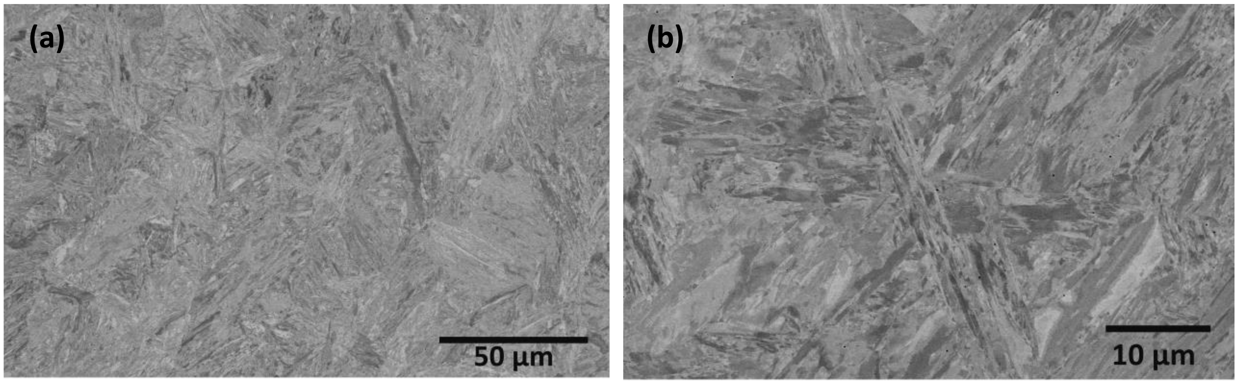

Figure 16. Representative backscattered electron micrographs of F/M Grade 91 steel: (a) low magnification and (b) high magnification.

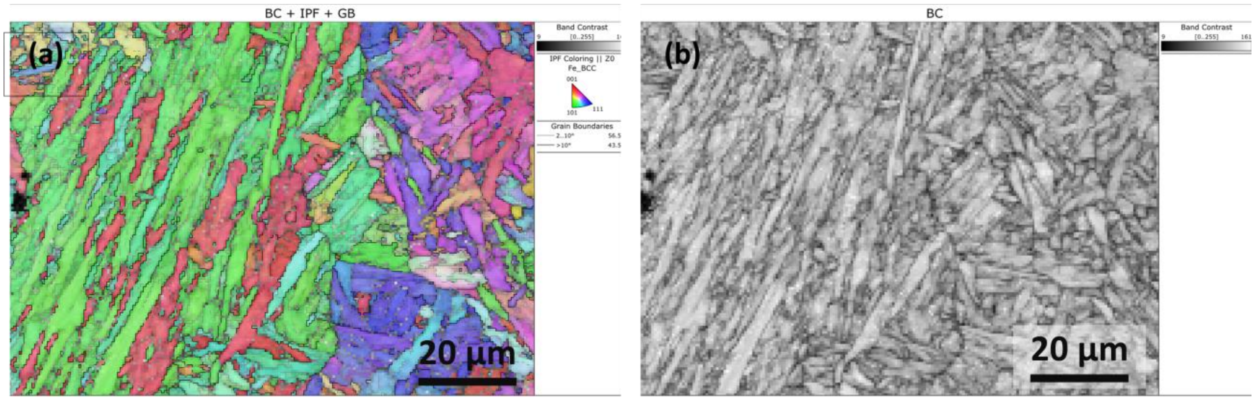

Figure 17. Representative EBSD orientation maps of Grade 91 steel: (a) inverse pole figure and grain boundary contrast and (b) band contrast.

5.4.2 X-Ray Diffraction Analysis of Grade 91 Steel

Figure 18 presents a representative XRD pattern collected from F/M G91 steel. The XRD pattern shows strong reflections from body-centered cubic (BCC) α-ferrite. The BCC peaks appear to be broad, indicating that the as-fabricated samples potentially contain a high density of dislocations causing a large amount of microstrain and a martensite phase (i.e., buried under the BCC peaks) (Robin, Sprouster et al. 2024).

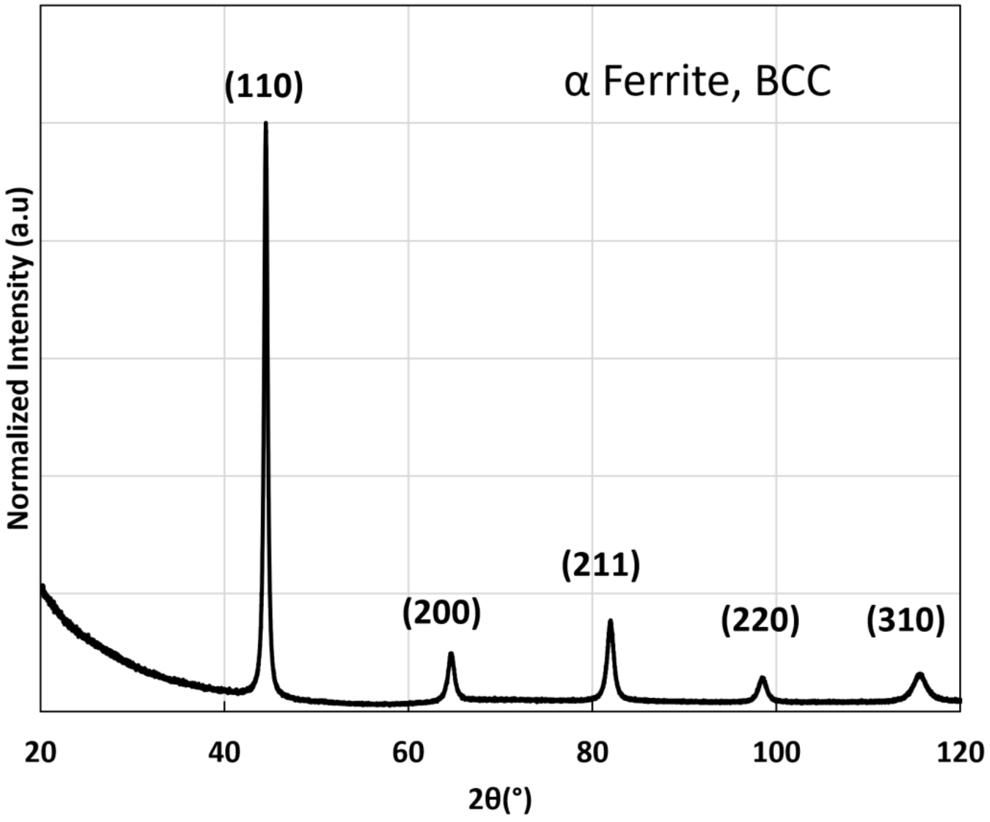

Figure 18. Representative XRD pattern collected from F/M Grade 91 steel.

5.4.3 Mechanical Properties of F/M Grade 91 Steel via the Vickers Hardness

The Vickers hardness of multiple samples of G91 steel was measured to understand the variation in hardness with the processing parameters. The average Vickers hardness collected from the samples with various laser powers and scan speeds for G91 steel is presented in Table 13. Figure 19 presents the variation in the Vickers hardness with the change in the laser power while the laser scan speed was kept constant for the G91 samples. It was observed that in general, the Vickers hardness tended to decrease as the laser power increased when the laser scan speed was kept constant. This could potentially be attributed to the increase in grain size due to higher laser power input.

Table 13. Average Vickers hardness of F/M Grade 91 steel.

Laser Power (W)	Scan Speed (mm/min)	Average Hardness
500	500	396.12 ± 19.46
500	600	398.08 ± 17.16
600	500	394.28 ± 14.45
600	700	390.9 ± 15.64
600	800	402.61 ± 19.02
700	500	381.24 ± 19.86
700	600	386.27 ± 13.84
700	700	386.21 ± 15.36
800	500	386.48 ± 15.68
800	600	386.91 ± 9.76
800	700	374.09 ± 30.48
800	800	384.00 ± 18.55
800	500	383.05 ± 16.93

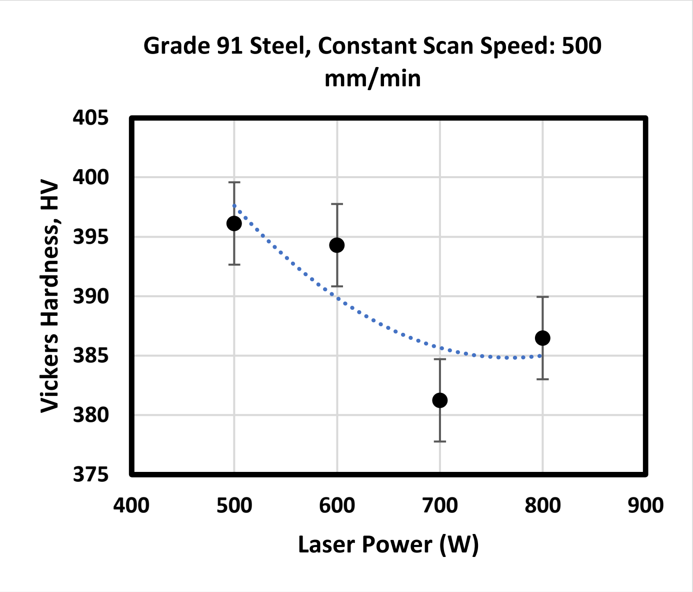

Figure 19. Variation in the Vickers hardness with the laser power at a constant scan speed for F/M Grade 91 steel.

5.4.4 Microstructural Analysis of Grade 92 Steel

Stitched optical micrographs of the XZ cross sections of the G92 samples produced with various laser powers and laser scan speeds are presented in Figure 20, allowing us to investigate the entire cross section. Some samples had a significantly higher number of pores, while few pores were also observed in some samples depending on the processing parameters, suggesting the importance optimizing the processing parameters to obtain a fully dense part. The relative densities of all samples were determined, and the porosity was observed to be 0.15%–2.53%. similar to the results for G91, this alloy also had the lowest porosity at a higher laser power. Hence, a laser power of 800 W and a scan speed of 500 mm/min were used to fabricate tensile bars [Figure 9(f)].

Figure 21 shows representative backscattered electron micrographs of F/M G92 steel at different magnifications. The microstructure primarily consists of fine and coarsened lath martensite. Representative EBSD orientation maps of F/M G92 steel are presented in Figure 22.

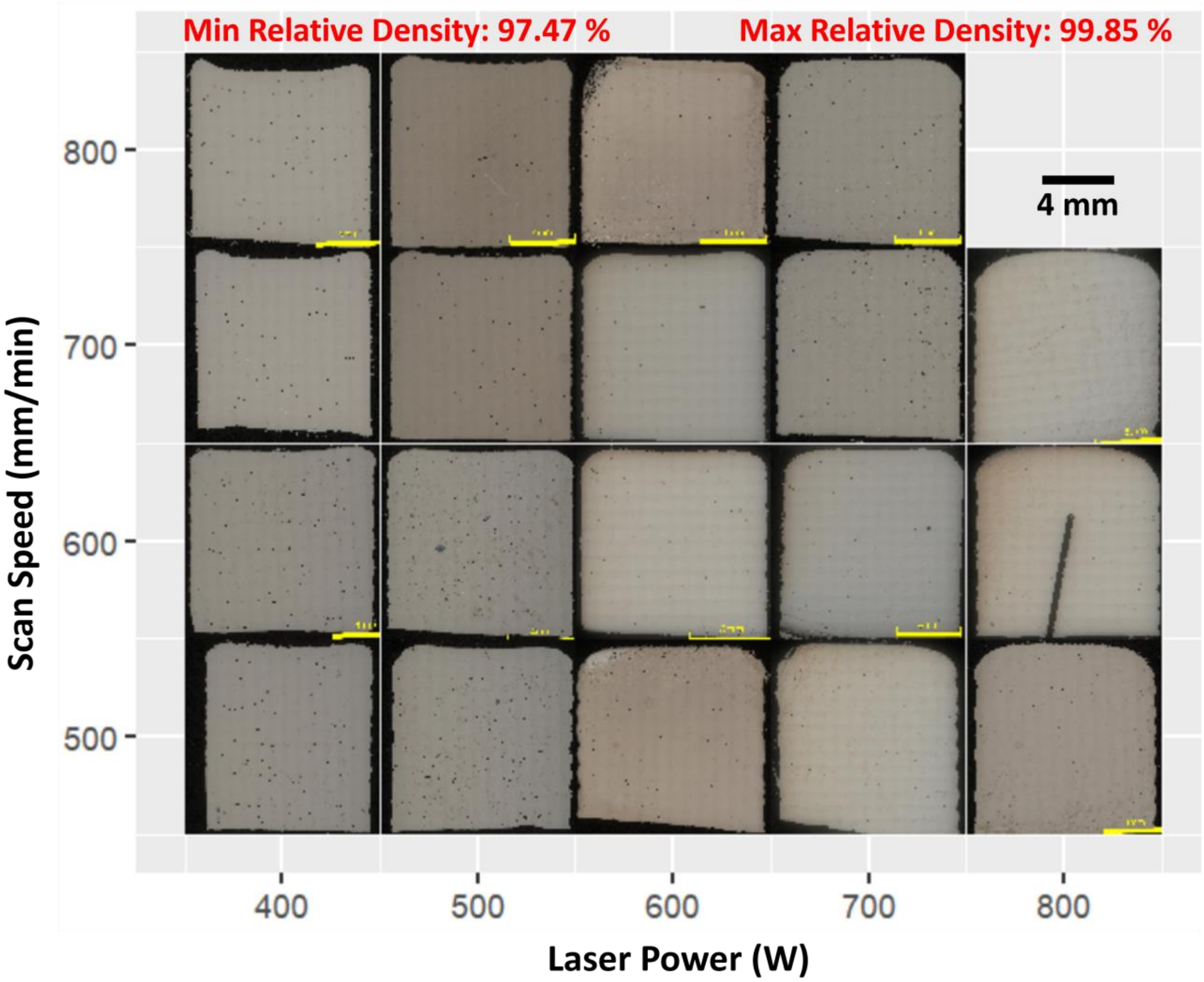

Figure 20. Stitched optical micrographs of the XZ cross sections of Grade 92 samples produced with various laser powers and laser scan speeds.

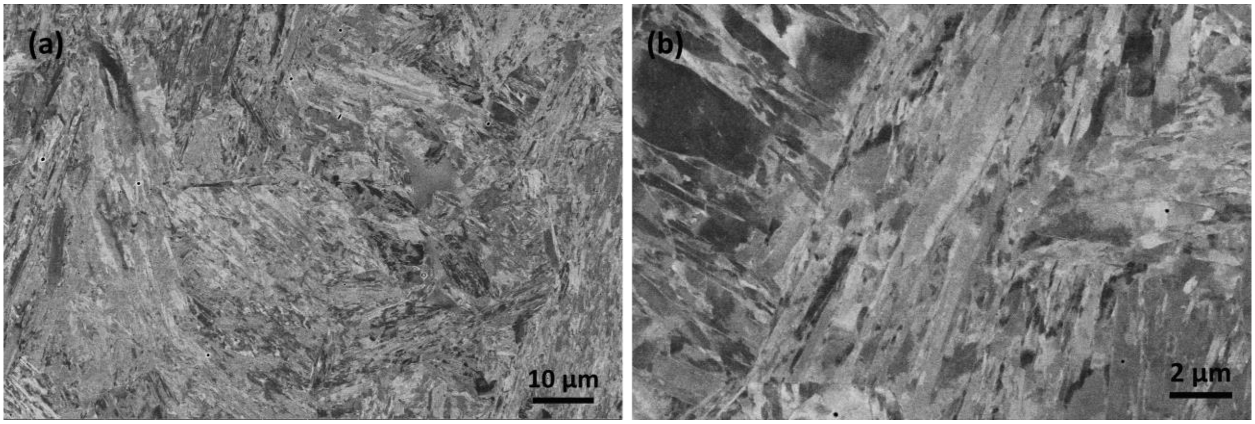

Figure 21. Representative backscattered electron micrographs of F/M Grade 92 steel: (a) low magnification and (b) high magnification.

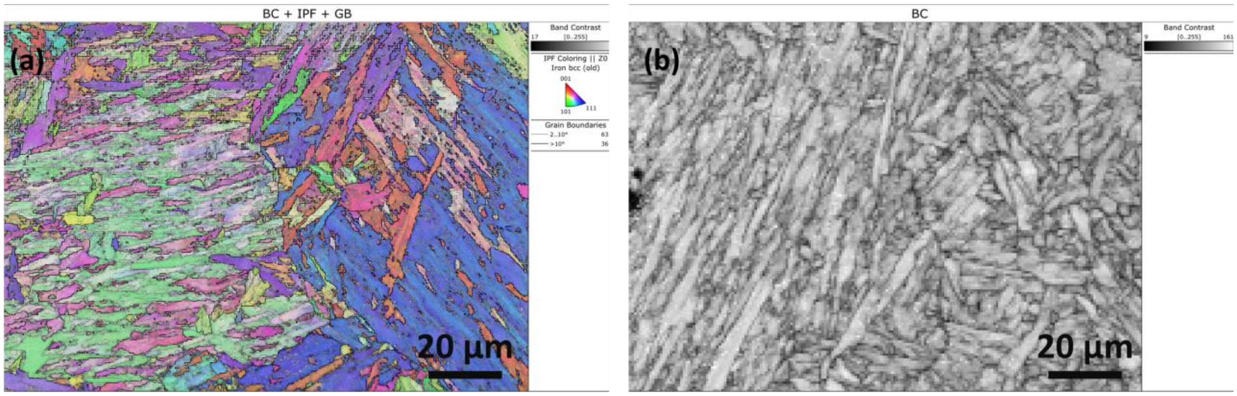

Figure 22. Representative EBSD orientation maps of Grade 92 steel: (a) inverse pole figure and (b) band contrast.

5.4.5 X-Ray Diffraction Analysis of Grade 92 Steel

An XRD pattern collected from a G92 sample is presented in Figure 23. The XRD pattern shows strong reflections from BCC α-ferrite. As G92 is an F/M steel, the martensite phase could potentially be buried under the BCC peaks, just like for G91. This scan was performed without a K_{beta} filter; hence, repetitive peaks were observed.

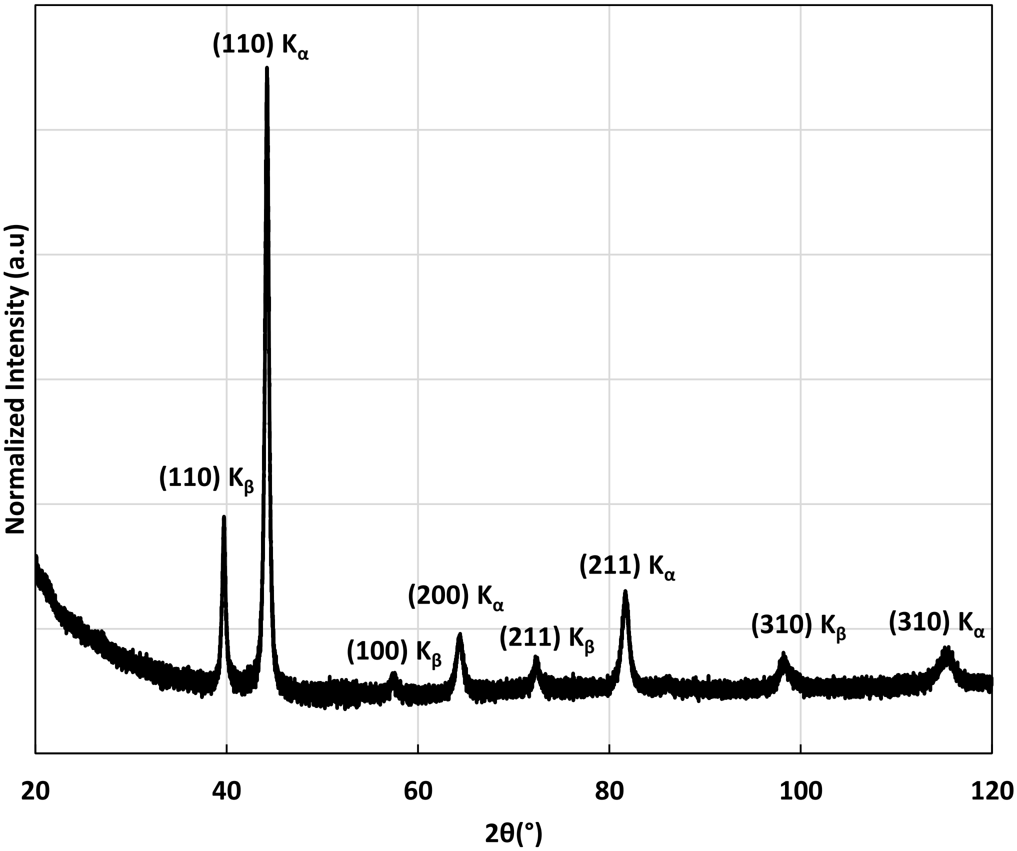

Figure 23. Representative XRD pattern collected from Grade 92 steel.

5.4.6 Mechanical Properties of F/M Grade 92 Steel via the Vickers Hardness

The Vickers hardness of multiple G92 samples was measured to understand the variation in the hardness with the processing parameters. The average Vickers hardness collected from the samples with various laser powers and scan speeds for G92 steel is presented in Table 14. Figure 24 presents the variation in the Vickers hardness with the change in the laser power while the laser scan speed was kept constant. Similar to G91 steel, it was observed that in general, the Vickers hardness tended to decrease as the laser power increased when the laser scan speed was kept constant, which could potentially be due to the increase grain size at a higher laser power.

Table 14. Average Vickers hardness of F/M Grade 92 steel.

Power (W)	Scan Speed (mm/min)	Average Hardness
500	500	429.04 ±18.86
500	600	432.05 ± 23.05
600	500	450.98 ± 19.90
600	700	436.06 ± 25.93
600	800	448.90 ± 15.93
700	500	422.21 ± 17.67
700	600	437.71 ± 13.24
700	700	441.60 ± 14.62
700	800	430.82 ± 11.50
800	500	413.24 ± 6.58
800	700	425.22 ± 12.41
800	500	419.97 ± 20.21

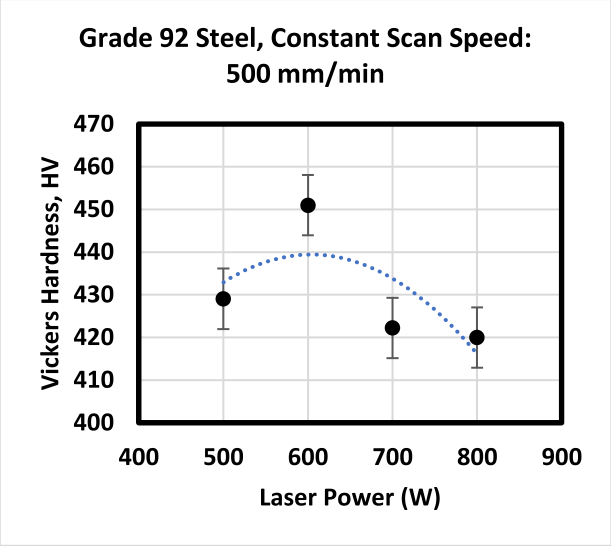

Figure 24. Variation in the Vickers hardness with the laser power at a constant scan speed for F/M Grade 92 steel.

5.4.7 Summary of the Vickers Hardness Observed

Table 15 presents a summary of the Vickers hardness observed for all three alloys along with the Vickers hardness values of similar steels reported in the literature.

Table 15. Summary of the Vickers hardness.

Category	Alloys	Fabrication Technique	Vickers Hardness	Ref.
Austenitic steels	SS304	AM-LPBF	254 ± 7.00	(Hartmann, Maloy and Komarasamy 2022)
	A709	AM-DED	219.27 ± 7.79	This study
	D-9	LPBF	189.3 ± 16.8	(Meher 2023)
F/M steels	Grade 91	AM-DED	398.08 ± 17.16	This study
	Grade 91	AM-Wire Arc	412 ± 23.04	(Robin, Sprouster et al. 2024)
	Grade 91	LPBF	281.4 ± 21.1	(Meher 2023)
	HT-9	LPBF	411.6 ± 24.7	(Meher 2023)
	Grade 92	AM-DED	432.05 ± 23.05	This study

6.0 Conclusion

This study investigated A709, G91, and G92 steels produced by DED. The findings are as follows:

1. **Printability study:**

   A chemical-composition-based ML model is used to predict the tendency of balling defect formation and the porosity in alloys in laser-based AM. The coupled ML and FLOW-3D results have provided insights into the impact of the alloy composition, particularly the carbon content, on the printability of SS316L and SS316H during AM processes.

2. **DED fabrication of stainless steels:**

   a. The A709 sample fabricated with a laser power of 400 W and a scan speed of 600 mm/min showed the highest density. In general, the porosity was 0.03%–1.1%; however, a few cracks were observed in some samples. The microstructure of austenitic A709 steel primarily consisted of a cellular dendritic structure decorated within the elongated grains. The XRD pattern revealed the presence of the austenitic FCC phase. The average Vickers hardness determined from the fully dense sample was observed to be 219.27 ± 7.79 HV.

   b. The G91 sample fabricated with a laser power of 500 W and a scan speed of 600 mm/min showed the highest density. The porosity was observed to be 0.03%–3.62%. The XRD pattern indicated strong reflections from BCC α-ferrite. It is assumed that the peaks corresponding to BCC ferrite and body-centered tetragonal (BCT) martensite overlapped because of broadening. The microstructure of G91 steel primarily consisted of fine and coarsened lath martensite. The average Vickers hardness determined from the fully dense sample was observed to be 398.08 ± 17.16 HV.

   c. The G92 sample fabricated with a laser power of 500 W and a scan speed of 700 mm/min showed the highest density. The porosity was observed to be 0.15%–2.53%. Like the G91 steel, the XRD pattern indicated strong reflections from BCC α-ferrite, and the peaks corresponding to a BCT martensite phase are assumed to be buried under the BCC peaks. The microstructure of G92 steel primarily consisted of fine and coarsened lath martensite. The average Vickers hardness determined from the fully dense sample was observed to be 432.05 ± 23.05 HV.

7.0 Deliverables

Publications:

[1] Ankit Roy, Andrew Swope, Ram Devanathan, and Isabella J. Van Rooyen. "Chemical composition-based machine learning model to predict defect formation in additive manufacturing." *Materialia* 33 (2024): 102041.

Conference Presentation:

[1] Isabella van Rooyen, Subhashish Meher, Asif Mahmud, Peter Renner, John Snitzer, Xiaoyuan Lou “Laser Directed Energy Deposition based Additive Manufacturing of Stainless Steels for Nuclear Applications: Process Development and Characterization”, MS&T 2024, Pittsburgh, PA.

[2] Subhashish Meher, Asif Mahmud, Peter Renner, German Valenzuela, John Snitzer, Xiaoyuan Lou, Isabella van Rooyen, “Additive Manufacturing and Characterization of A709 Stainless Steels for Nuclear Applications”, TMS 2025, Las Vegas, NV.

8.0 Future Work

1. The Flow-3D software will be coupled with ML for extensive research on the role of the chemical composition on the printability in the DED process.
2. The FY-25 work will focus on DED prints of A709 and G92 for mechanical testing. Further optimization of process parameter will take place based on this FY results. The microstructural and mechanical testing data will be compared with that of LPBF and conventionally fabricated parts.
3. For DED A709, solution anneal treatment at a minimum temperature of 1150°C for 10 hours will be implemented followed by air cooling. The precipitation treatment (PT) will be carried out at 775°C for 10 hours in air followed by air cooling. (Mahajan, Wang et al. 2023). Future study will focus on room-temperature tensile testing for DED fabricated A709 and G92 alloy. In addition, detailed electron microscopy analyses after the heat treatments and tensile testing also fall within the work scope.
4. For DED G92, solution anneal treatment at 1080°C will be carried out. G92 is being pursued because of its improved properties compared to G91. Detailed microstructural analysis after heat treatments and mechanical testing will be carried out.

9.0 References

Designation: A213/A213M − 19a Standard Specification for Seamless Ferritic and Austenitic Alloy-Steel Boiler, Superheater, and Heat-Exchanger Tubes 1.

Abe, F. (2008). "Precipitate design for creep strengthening of 9% Cr tempered martensitic steel for ultra-supercritical power plants." Science and Technology of Advanced Materials **9**.

Abe, F. (2014). Grade 91 heat-resistant martensitic steel.

Aboulkhair, N. T., N. M. Everitt, I. Ashcroft and C. Tuck (2014). "Reducing porosity in AlSi10Mg parts processed by selective laser melting." Additive Manufacturing **1-4**: 77-86.

Adjamskyi, S. V., G. A. Kononenko and R. V. Podolskyi (2020). "Influence of technological parameters of slm-process on porosity of metal products." The Paton Welding Journal **2020**(10): 13-18.

Alomari, A. S., N. Kumar and K. L. Murty (2018). "Enhanced ductility in dynamic strain aging regime in a Fe-25Ni-20Cr austenitic stainless steel." Materials Science & Engineering A **729**: 157-160.

Amar, E., V. Popov, V. Sharma, S. Andreev Batat, D. Halperin and N. Eliaz (2023). "Response Surface Methodology (RSM) Approach for Optimizing the Processing Parameters of 316L SS in Directed Energy Deposition." Materials **16**: 7253.

Ang, Y., S. L. Sing and J. Lim (2022). "Process study for directed energy deposition of 316L stainless steel with TiB2 metal matrix composites." Materials Science in Additive Manufacturing **1**: 13.

Angelone, R., A. Caggiano, R. Teti, A. Spierings, A. Staub and K. Wegener (2020). "Bio-intelligent selective laser melting system based on convolutional neural networks for in-process fault identification." Procedia CIRP **88**: 612-617.

Armas, A. F., M. Avalos, I. Alvarez-Armas, C. Peterson and R. Schmitt (1998). "Dynamic strain ageing evidences during low cycle fatigue deformation in ferritic-martensitic stainless steels." Journal of Nuclear Materials **258-263**: 124-1208.

ASTM (2023). Standard Specification for Seamless Ferritic and Austenitic Alloy-Steel Boiler Superheater, and Heat-Exchanger Tubes. ASTM A213/A213M-23.

Atli, K., H. Boon, R. Seede, B. Zhang, A. Elwany, R. Arroyave and I. Karaman (2021). "Laser-based additive manufacturing of a binary Ni-5 wt.% Nb alloy." Journal of Manufacturing Processes **62**: 720-728.

Attar, H., M. Calin, L. C. Zhang, S. Scudino and J. Eckert (2014). "Manufacture by selective laser melting and mechanical behavior of commercially pure titanium." Materials Science and Engineering: A **593**: 170-177.

Azinpour, E., R. Darabi, J. Cesar de Sa, A. Santos, J. Hodek and J. Dzugan (2020). "Fracture analysis in directed energy deposition (DED) manufactured 316L stainless steel using a phase-field approach." Finite Elements in Analysis and Design **177**: 103417.

Bansod, A., S. Shukla, G. Gabriel and J. Verma (2023). "Influence of filler wire on metallurgical, mechanical, and corrosion behaviour of 430 ferritic stainless steel using a fusion welding process." Materials Research Express **10**.

Baumgartl, H., J. Tomas, R. Buettner and M. Merkel (2020). "A deep learning-based model for defect detection in laser-powder bed fusion using in-situ thermographic monitoring." Progress in Additive Manufacturing **5**(3): 277-285.

Benarji, K., Y. R. Kumar, C. Paul, A. Jinoop and K. Bindra (2020). "Parametric investigation and characterization on SS316 built by laser-assisted directed energy deposition." Proceedings of the Institution of Mechanical Engineers, Part L: Journal of Materials: Design and Applications **234**(3): 452-466.

Breiman, L. (2001). "Random forests." Machine learning **45**: 5-32.

Bronkhorst, C. A., J. R. Mayeur, V. Livescu, R. Pokharel, D. W. Brown and G. T. Gray (2019). "Structural representation of additively manufactured 316L austenitic stainless steel." International Journal of Plasticity **118**: 70-86.

Butler, K. T., D. W. Davies, H. Cartwright, O. Isayev and A. Walsh (2018). "Machine learning for molecular and materials science." Nature **559**(7715): 547-555.

Cabet, C., F. Dalle, E. Gaganidze, J. Henry and H. Tanigawa (2019). "Ferritic-martensitic steels for fission and fusion applications." Journal of Nuclear Materials **523**: 510-537.

Caggiano, A., J. Zhang, V. Alfieri, F. Caiazzo, R. Gao and R. Teti (2019). "Machine learning-based image processing for on-line defect recognition in additive manufacturing." CIRP annals **68**(1): 451-454.

Carroll, A. M. B. B. E. (2015). "Review of Mechanical Properties of Ti-6Al-4V Made by Laser-Based Additive Manufacturing Using Powder Feedstock."

Chen, Z., Z. Wei, P. Wei, S. Chen, B. Lu, J. Du, J. Li and S. Zhang (2017). "Experimental Research on Selective Laser Melting AlSi10Mg Alloys: Process, Densification and Performance." Journal of Materials Engineering and Performance **26**(12): 5897-5905.

Davtalab, O., A. Kazemian, X. Yuan and B. Khoshnevis (2022). "Automated inspection in robotic additive manufacturing using deep learning for layer deformation detection." Journal of Intelligent Manufacturing **33**(3): 771-784.

Dayhoff, J. E. (1990). Neural network architectures: an introduction, Van Nostrand Reinhold Co.

de Lima, M. S. F. and S. Sankaré (2014). "Microstructure and mechanical behavior of laser additive manufactured AISI 316 stainless steel stringers." Materials & Design **55**: 526-532.

DebRoy, T., T. Mukherjee, J. Milewski, J. Elmer, B. Ribic, J. Blecher and W. Zhang (2019). "Scientific, technological and economic issues in metal printing and their solutions." Nature materials **18**(10): 1026-1032.

DebRoy, T., T. Mukherjee, H. Wei, J. Elmer and J. Milewski (2021). "Metallurgy, mechanistic models and machine learning in metal printing." Nature Reviews Materials **6**(1): 48-68.

DebRoy, T., H. Wei, J. Zuback, T. Mukherjee, J. Elmer, J. Milewski, A. M. Beese, A. d. Wilson-Heid, A. De and W. Zhang (2018). "Additive manufacturing of metallic components–process, structure and properties." Progress in Materials Science **92**: 112-224.

Denlinger, E., J. Heigel, P. Michaleris and T. A. Palmer (2015). "Effect of inter-layer dwell time on distortion and residual stress in additive manufacturing of titanium and nickel alloys." Journal of Materials Processing Technology **215**: 123-131.

Ding, R., J. Yan, H. Li, S. Yu, A. Rabiei and P. Bowen (2019). "Deformation microstructure and tensile properties of Alloy 709 at different temperatures." Materials and Design.

Dong, P., F. Vecchiato, Z. Yang, P. A. Hooper and M. R. Wenman (2021). "The effect of build direction and heat treatment on atmospheric stress corrosion cracking of laser powder bed fusion 316L austenitic stainless steel." Additive Manufacturing **40**.

Du, Y., T. Mukherjee and T. DebRoy (2021). "Physics-informed machine learning and mechanistic modeling of additive manufacturing to reduce defects." Applied Materials Today **24**: 101123.

Eftink, B. P., D. A. Vega, O. E. Atwani, D. J. Sprouster, Y. S. J. Yoo, T. E. Steckley, E. Aydogan, C. M. Cady, M. Al-Sheikhly, T. J. Lienert and S. A. Maloy (2021). "Tensile Properties and microstructure of additively manufactured Grade 91 steel for nuclear applications." Journal of Nuclear Materials **544**.

El-Atwani, O., B. P. Eftink, C. M. Cady, D. R. Coughlin, M. M. Schneider and S. A. Maloy (2021). "Enhanced mechanical properties of additive manufactured Grade 91 steel." Scripta Materialia **199**.

Enneti, R. K., R. Morgan and S. V. Atre (2018). "Effect of process parameters on the Selective Laser Melting (SLM) of tungsten." International Journal of Refractory Metals and Hard Materials **71**: 315-319.

Era, I. Z. and Z.-C. Liu (2021). "Effect of process parameters on tensile properties of SS 316 prepared by directional energy deposition." Procedia CIRP **103**: 115-121.
Fathizadan, S., F. Ju and Y. Lu (2021). "Deep representation learning for process variation management in laser powder bed fusion." Additive Manufacturing **42**: 101961.
Feenstra, D., V. Cruz, X. Gao, A. Molotnikov and N. Birbilis (2020). "Effect of Build Height on the Properties of Large Format Stainless Steel 316L Fabricated via Directed Energy Deposition." Additive Manufacturing **34**: 101205.
Feng, J., P. Zhang, Z. Jia, Z. Yu, C. Fang, H. Yan, H. Shi, Y. Tian and F. Xie (2022). "Laser additive manufacturing and post-heat treatment on microstructure and mechanical properties of 9Cr steel." International Journal of Pressure Vessels and Piping **198**.
Fetni, S., T. M. Enrici, T. Niccolini, H. S. Tran, O. Dedry, L. Duchêne, A. Mertens and A. M. Habraken (2021). "Thermal model for the directed energy deposition of composite coatings of 316L stainless steel enriched with tungsten carbides." Materials & Design **204**: 109661.
Fousova, M., D. Vojtech, J. Kubasek, E. Jablonska and J. Fojt (2017). "Promising characteristics of gradient porosity Ti-6Al-4V alloy prepared by SLM process." J Mech Behav Biomed Mater **69**: 368-376.
Frazier, W. E. (2014). "Metal Additive Manufacturing: A Review." Journal of Materials Engineering and Performance **23**: 1917-1928.
Friedman, J. H. (2001). "Greedy function approximation: a gradient boosting machine." Annals of statistics: 1189-1232.
Fukushima, K. (1975). "Cognitron: A self-organizing multilayered neural network." Biological cybernetics **20**(3): 121-136.
Gong, H., K. Rafi, H. Gu, G. D. Janaki Ram, T. Starr and B. Stucker (2015). "Influence of defects on mechanical properties of Ti–6Al–4V components produced by selective laser melting and electron beam melting." Materials & Design **86**: 545-554.
Gorelik, M. (2017). "Additive manufacturing in the context of structural integrity." International Journal of Fatigue **94**: 168-177.
Gräning, T. and N. Sridharan (2022). "Benchmarking a 9Cr-2WVTa Reduced Activation Ferritic Martensitic Steel Fabricated via Additive Manufacturing." Metals **12**: Medium: ED; Size: Article No. 342.
Gräning, T. and N. Sridharan (2022). "Benchmarking a 9Cr-2WVTa Reduced Activation Ferritic Martensitic Steel Fabricated via Additive Manufacturing." Metals **12**(2): 342.
Gu, P., T. Qi, L. Chen, T. Ge and X. Ren (2022). "Manufacturing and analysis of VNbMoTaW refractory high-entropy alloy fabricated by selective laser melting." International Journal of Refractory Metals and Hard Materials **105**: 105834.
Guo, P., B. Zou, C. Huang and H. Gao (2017). "Study on microstructure, mechanical properties and machinability of efficiently additive manufactured AISI 316L stainless steel by high-power direct laser deposition." Journal of Materials Processing Technology **240**: 12-22.
Hartmann, T., S. Maloy and M. Komarasamy (2022). Material Scorecards, Phase 2 Pacific Northwest National Laboratory.
Hatakeyama, T., K. Sawada, M. Suzuki and M. Watanabe (2023). "Microstructure development of modified 9Cr-1Mo steel during laser powder bed fusion and heat treatment." Additive Manufacturing **61**.
Henry, J. and S. A. Maloy (2017). Irradiation-resistant ferritic and martensitic steels as core materials for Generation IV nuclear reactors. Structural Materials for Generation IV Nuclear Reactors**:** 329-355.
Hossein Nedjad, S., M. Yildiz and A. Saboori (2023). "Solidification behaviour of austenitic stainless steels during welding and directed energy deposition." Science and Technology of Welding and Joining **28**(1): 1-17.
Hou, Y., H. Su, H. Zhang, X. Wang and C. Wang (2021). "Fabricating homogeneous fecocrni high-entropy alloys via slm in situ alloying." Metals **11**(6): 942.

Hwa, Y., C. S. Kumai, T. M. Devine, N. Yang, J. K. Yee, R. Hardwick and K. Burgmann (2021). "Microstructural banding of directed energy deposition-additively manufactured 316L stainless steel." Journal of Materials Science & Technology **69**: 96-105.

Ikeda, T., M. Yonehara, T.-T. Ikeshoji, T. Nobuki, M. Hatate, K. Kuwabara, Y. Otsubo and H. Kyogoku (2021). "Influences of process parameters on the microstructure and mechanical properties of CoCrFeNiTi based high-entropy alloy in a laser powder bed fusion process." Crystals **11**(5): 549.

Izadi, M., A. Farzaneh, I. Gibson and B. F. Rolfe (2017). The effect of process parameters and mechanical properties of direct energy deposited stainless steel 316.

Kaufmann, K. and K. S. Vecchio (2020). "Searching for high entropy alloys: A machine learning approach." Acta Materialia **198**: 178-222.

Khan, M. F., A. Alam, M. A. Siddiqui, M. S. Alam, Y. Rafat, N. Salik and I. Al-Saidan (2021). "Real-time defect detection in 3D printing using machine learning." Materials Today: Proceedings **42**: 521-528.

Kim, J., B. Kang and S.-W. Lee (2019). "An experimental study on microstructural characteristics and mechanical properties of stainless-steel 316L parts using directed energy deposition (DED) process." Journal of Mechanical Science and Technology **33**: 5731-5737.

Kimura, K., K. Kwak, S. Nambu and T. Koseki (2020). "Nondestructive evaluation of macro segregation in creep strength enhanced 9Cr-1Mo-V-Nb steel." Scripta Materialia **188**: 179-182.

Klueh, R. L., A. T. Nelson and Oak Ridge National Laboratory (2007). "Ferritic/martensitic steels for next-generation reactors." Journal of Nuclear Materials **371**: 37-52.

Lashgari, H. R., Y. Xue, C. Onggowarsito, C. Kong and S. Li (2020). "Microstructure, Tribological Properties and Corrosion Behaviour of Additively Manufactured 17-4PH Stainless Steel: Effects of Scanning Pattern, Build Orientation, and Single vs. Double scan." Materials Today Communications **25**.

Li, C., Z. Y. Liu, X. Y. Fang and Y. B. Guo (2018). "Residual Stress in Metal Additive Manufacturing." Science Direct **71**: 348-353.

Li, M., K. Natesan, W. Chen and Y. Momozaki Sodium Compatibility of Recently-Developed Optimized Grade 92 Steel for Advanced Fast Reactors. Argonne National Laboratory, Department of Energy.

Li, M., Z. Zeng, Y. Momozaki, D. L. Rink and J. Listwan (2021). Progress Report on Performance of A709 and G91 Steels in Sodium. Argonne National Laboratory, Department of Energy.

Li, R., P. Niu, T. Yuan, P. Cao, C. Chen and K. Zhou (2018). "Selective laser melting of an equiatomic CoCrFeMnNi high-entropy alloy: Processability, non-equilibrium microstructure and mechanical property." Journal of Alloys and Compounds **746**: 125-134.

Li, W., M. N. Kishore, R. Zhang, N. Bian, H. Lu, Y. Li, D. Qian and X. Zhang (2023). "Comprehensive studies of SS316L/IN718 functionally gradient material fabricated with directed energy deposition: Multi-physics & multi-materials modelling and experimental validation." Additive Manufacturing **61**: 103358.

Li, X., X. Jia, Q. Yang and J. Lee (2020). "Quality analysis in metal additive manufacturing with deep learning." Journal of Intelligent Manufacturing **31**: 2003-2017.

Lienert, T. J. and S. A. Maloy (2017). Laser Additive Manufacturing of F/M Steels for Radiation Tolerant Nuclear Components. United States**:** Medium: ED; Size: 19 p.

Lin, P.-Y., F.-C. Shen, K.-T. Wu, S.-J. Hwang and H.-H. Lee (2020). "Process optimization for directed energy deposition of SS316L components." The International Journal of Advanced Manufacturing Technology **111**: 1-14.

Lou, X., P. L. Andresen and R. B. Rebak (2018). "Oxide inclusions in laser additive manufactured stainless steel and their effects on impact toughness and stress corrosion cracking behavior." Journal of Nuclear Materials **499**: 182-190.

M, K. and V. Senthilkumar (2021). "Experimental characterization of stainless steel 316L alloy fabricated with combined powder bed fusion and directed energy deposition." Welding in the World **65**: 1-16.
Ma, M., Z. Wang, W. Dengzhi and X. Zeng (2013). "Control of shape and performance for direct laser fabrication of precision large-scale metal parts with 316L Stainless Steel." Optics Laser Technology **45**: 209-216.
Ma, M., Z. Wang and X. Zeng (2016). "A comparison on metallurgical behaviors of 316L stainless steel by selective laser melting and laser cladding deposition." Materials Science and Engineering: A **685**.
Mahajan, H. P., Y. Wang, Z. Feng, X. Zhang and T.-L. Sham (2023). A summary of the mechanical properties data developed in FY 2023 by ANL, INL and ORNL to support the data package development for the A709 Code Case. United States**:** Medium: ED.
Mahmood, M. A., F. G. Alabtah, Y. Al Hamidi and M. Khraisheh (2023). "On Laser Additive Manufacturing of High-entropy Alloys: A Critical Assessment of In-situ Monitoring Techniques and Their Suitability." Materials & Design: 111658.
Mantri, S. A. and X. Zhang (2023). Evaluation of LPBF Steels for Nuclear Applications. Argonne National Laboratory, Department of Energy.
Marya, M., V. Singh, S. Marya and J. Y. Hascoet (2015). "Microstructural Development and Technical Challenges in Laser Additive Manufacturing: Case Study with a 316L Industrial Part." Metallurgical and Materials Transactions B **46**(4): 1654-1665.
Meher, S. (2023). Evaluation of printability methodologies and feasibility to down select LPBF steel and other materials for nuclear applications.
Mostafaei, A., C. Zhao, Y. He, S. R. Ghiaasiaan, B. Shi, S. Shao, N. Shamsaei, Z. Wu, N. Kouraytem and T. Sun (2022). "Defects and anomalies in powder bed fusion metal additive manufacturing." Current Opinion in Solid State and Materials Science **26**(2): 100974.
Mueller, T., A. G. Kusne and R. Ramprasad (2016). "Machine learning in materials science: Recent progress and emerging applications." Reviews in computational chemistry **29**: 186-273.
Niu, P., R. Li, K. Gan, T. Yuan, S. Xie and C. Chen (2021). "Microstructure, properties, and metallurgical defects of an equimolar CoCrNi medium entropy alloy additively manufactured by selective laser melting." Metallurgical and Materials Transactions A **52**: 753-766.
Niu, P., R. Li, S. Zhu, M. Wang, C. Chen and T. Yuan (2020). "Hot cracking, crystal orientation and compressive strength of an equimolar CoCrFeMnNi high-entropy alloy printed by selective laser melting." Optics & Laser Technology **127**.
Poorganji, B., E. Ott, R. Kelkar, A. Wessman and M. Jamshidinia (2020). "Review: Materials Ecosystem for Additive Manufacturing Powder Bed Fusion Processes." JOM **72**: 561-576.
Probst, P. and A.-L. Boulesteix (2017). "To tune or not to tune the number of trees in random forest." The Journal of Machine Learning Research **18**(1): 6673-6690.
Rangaswamy, P., M. L. Griffith, T. M. Holden, M. B. Prime and R. B. Rogge (2005). "Residual stresses in LENS components using neutron diffraction and contour method." Materials Science & Engineering A **399**: 72-83.
Robin, I. K., D. J. Sprouster, N. Sridharan, L. L. Snead and S. J. Zinkle (2024). "Synchrotron based investigation of anisotropy and microstructure of wire arc additive manufactured Grade 91 steel." Journal of Materials Research and Technology-Jmr&T **29**: 5010-5021.
Romano, S., A. Brandao, J. Gumpinger, M. Gschweitl and S. Beretta (2017). "Qualification of AM parts: Extreme value statistics applied to tomographic measurements." Materials and Design **131**: 32-48.
Roy, A., R. Devanathan, D. D. Johnson and G. Balasubramanian (2022). "Grain-size effects on the deformation in nanocrystalline multi-principal element alloy." Materials Chemistry and Physics **277**: 125546.
Roy, A., J. Munshi and G. Balasubramanian (2021). "Low energy atomic traps sluggardize the diffusion in compositionally complex refractory alloys." Intermetallics **131**: 107106.

Roy, A., P. Singh, G. Balasubramanian and D. D. Johnson (2022). "Vacancy formation energies and migration barriers in multi-principal element alloys." Acta Materialia: 117611.
Saboori, A., G. Piscopo, M. Lai, A. Salmi and S. Biamino (2020). "An investigation on the effect of deposition pattern on the microstructure, mechanical properties and residual stress of 316L produced by Directed Energy Deposition." Materials Science and Engineering: A **780**: 139179.
Samuha, S., J. Bickel, T. Mukherjee, T. DebRoy, T. J. Lienert, S. A. Maloy, C. R. Lear and P. Hosemann (2023). "Mechanical performance and microstructure of the grade 91 stainless steel produced via Directed Energy deposition laser technique." Materials & Design **227**: 111804.
Sarswat, P. K., S. Sarkar, A. Murali, W. Huang, W. Tan and M. L. Free (2019). "Additive manufactured new hybrid high entropy alloys derived from the AlCoFeNiSmTiVZr system." Applied Surface Science **476**: 242-258.
Sau, M., E. D. Hintsala, Y. Chen, D. D. Stauffer, S. A. Maloy, B. P. Eftink, T. J. Lienert and N. A. Mara (2022). "High-Throughput Nanoindentation Mapping of Additively Manufactured T91 Steel." JOM **74**(4): 1469-1476.
Sciammarella, F. and B. Salehi Najafabadi (2018). "Processing Parameter DOE for 316L Using Directed Energy Deposition." Journal of Manufacturing and Materials Processing **2**: 61.
Scime, L. and J. Beuth (2018). "A multi-scale convolutional neural network for autonomous anomaly detection and classification in a laser powder bed fusion additive manufacturing process." Additive Manufacturing **24**: 273-286.
Seran, J. L., J. C. Brachet and A. Alamo (2001). Ferritic-Martensitic Steels for Fast Reactor Cores. Encyclopedia of Materials: Science and Technology, Elsevier Science Ltd.**:** 2863-2866.
Sham, T.-L. (2022). Alloy 709 Advanced Austenitic Stainless Steel. United States**:** Medium: ED.
Sham, T.-L., R. E. Bass, Y. Wang and X. Zhang (2022). A709 Qualification Plan Update and Mechanical Properties Data Assessment. United States**:** Medium: ED.
Shrestha, T., S. Alsagabi, I. Charit, G. Potirniche and M. Glazoff (2015). "Effect of Heat Treatment on Microstructure and Hardness of Grade 91 Steel." Metals **5**: 131-149.
Singhal, T. S., J. K. Jain, M. Kumar, V. Bhojak, K. K. Saxena, D. Buddhi and C. Prakash (2023). "A comprehensive comparative review: welding and additive manufacturing." International Journal on Interactive Design and Manufacturing **18**: 1829-1843.
Smith, D. S., N. J. Lybeck, J. K. Wright and R. N. Wright (2017). "Thermophysical properties of Alloy 709." Nuclear Engineering and Design **322**: 331-335.
Smith, T., J. Sugar, C. San Marchi and J. Schoenung (2018). "Strengthening Mechanisms in Directed Energy Deposited Austenitic Stainless Steel." Acta Materialia **164**.
Snow, Z., B. Diehl, E. W. Reutzel and A. Nassar (2021). "Toward in-situ flaw detection in laser powder bed fusion additive manufacturing through layerwise imagery and machine learning." Journal of Manufacturing Systems **59**: 12-26.
Sreeramagiri, P., A. Roy and G. Balasubramanian (2021). "Effect of cooling rate on the phase formation of AlCoCrFeNi high-entropy alloy." Journal of Phase Equilibria and Diffusion **42**(5): 772-780.
Sridharan, N. and K. Field (2019). "A Road Map for the Advanced Manufacturing of Ferritic-Martensitic Steels." Fusion Science and Technology **75**: 264-274.
Sridharan, N., M. N. Gussev and K. Field (2019). "Performance of ferritic/martensitic steel for nuclear reactor applications fabricated using additive manufacturing." Journal of Nuclear Materials **521**: 45-55.
Sridharan, N., M. N. Gussev and K. G. Field (2019). "Performance of a ferritic/martensitic steel for nuclear reactor applications fabricated using additive manufacturing." Journal of Nuclear Materials **521**: 45-55.
Sun, K., W. Peng, L. Yang and L. Fang (2020). "Effect of SLM processing parameters on microstructures and mechanical properties of Al0. 5CoCrFeNi high entropy alloys." Metals **10**(2): 292.

Tan, L., W. Zhong, Y. Yang, K. G. Field, N. Sridharan and A. T. Nelson (2022). "Creep behavior of an additively manufactured 9Cr steel in the as-built condition." Journal of Nuclear Materials **570**: 153943.
Tang, X., H. Zhang, Z. Zhu, P. Xue, L. Wu, F. Liu, D. Ni, B. Xiao and Z. Ma (2023). "Dual-phase synergistic deformation characteristics and strengthening mechanism of AlCoCrFeNi2. 1 eutectic high entropy alloy fabricated by laser powder bed fusion." Journal of Materials Science & Technology **150**: 75-85.
Trillo, E. and L. Murr (1998). "Effects of carbon content, deformation, and interfacial energetics on carbide precipitation and corrosion sensitization in 304 stainless steel." Acta materialia **47**(1): 235-245.
Vaughan, M., M. Elverud, J. Ye, R. Seede, S. Gibbons, P. Flater, B. Gaskey, R. Arróyave, A. Elwany and I. Karaman (2023). "Development of a Process Optimization Framework for Fabricating Fully Dense Advanced High Strength Steels using Laser Directed Energy Deposition." Additive Manufacturing **67**: 103489.
Villaret, F., X. Boulnat, P. Aubry, J. Zollinger, D. Fabregue and Y. de Carlan (2021). "Modelling of delta ferrite to austenite phase transformation kinetics in martensitic steels: Application to rapid cooling in additive manufacturing." Materiala **18**.
Villaret, F., X. Boulnat, P. Aubry, J. Zollinger, D. Fabrègue and Y. de Carlan (2021). "Modelling of delta ferrite to austenite phase transformation kinetics in martensitic steels: Application to rapid cooling in additive manufacturing." Materialia **18**: 101157.
Wang, F., T. Yuan, R. Li, S. Lin, P. Niu and V. Cristino (2023). "Effect of Mo on the morphology, microstructure and mechanical properties of NbTa0. 5TiMox refractory high entropy alloy fabricated by laser powder bed fusion using elemental mixed powders." International Journal of Refractory Metals and Hard Materials: 106107.
Wang, Y., P. Hou, R. E. Bass, X. Zhang and T. L. Sham (2022). Interim Mechanical Properties Data from FY2022 ORNL Testing of A709 with Precipitation Treatment for ASME Code Case Data Package. United States**:** Medium: ED; Size: 39 p.
Wang, Z., T. Palmer and A. Beese (2016). "Effect of processing parameters on microstructure and tensile properties of austenitic stainless steel 304L made by directed energy deposition additive manufacturing." Acta Materialia **110**: 226-235.
Wei, H., T. Mukherjee, W. Zhang, J. Zuback, G. Knapp, A. De and T. DebRoy (2021). "Mechanistic models for additive manufacturing of metallic components." Progress in Materials Science **116**: 100703.
Weng, F., S. Gao, J. Jiang, J. Wang and P. Guo (2019). "A novel strategy to fabricate thin 316L stainless steel rods by continuous directed energy deposition in Z direction." Additive Manufacturing **27**: 474-481.
Westphal, E. and H. Seitz (2021). "A machine learning method for defect detection and visualization in selective laser sintering based on convolutional neural networks." Additive Manufacturing **41**: 101965.
Whitt, A., R. Seede, J. Ye, M. Elverud, M. Vaughan, A. Elwany, R. Arroyave and I. Karaman (2023). "A process optimization framework for laser direct energy deposition: Densification, microstructure, and mechanical properties of an Fe Cr alloy." Journal of Manufacturing Processes **85**: Medium: X; Size: p. 434-449.
Whitt, A., R. Seede, J. Ye, M. Elverud, M. Vaughan, A. Elwany, R. Arroyave and I. Karaman (2023). "A process optimization framework for laser direct energy deposition: Densification, microstructure, and mechanical properties of an FeCr alloy." Journal of Manufacturing Processes **85**: 434-449.
Wolf, M. and W. Kurz (1981). "The effect of carbon content on solidification of steel in the continuous casting mold." Metallurgical Transactions B **12**: 85-93.

Xia, Z., J. Xu, J. Shi, T. Shi, C. Sun and D. Qiu (2020). "Microstructure evolution and mechanical properties of reduced activation steel manufactured through laser directed energy deposition." Additive Manufacturing **33**: 101114.

Yadollahi, A., N. Shamsaei, Y. Hammi and M. F. Horstemeyer (2016). "Quantification of tensile damage evolution in additive manufactured austenitic stainless steels." Materials Science and Engineering: A **657**: 399-405.

Yadollahi, A., N. Shamsaei, S. M. Thompson and D. W. Seely (2015). "Effects of process time interval and heat treatment on the mechanical and microstructural properties of direct laser deposited 316L stainless steel." Materials Science and Engineering: A **644**: 171-183.

Yang, D., X. Kan, P. Gao, Y. Zhao, Y. Yin, Z. Zhao and J. Sun (2021). "Influence of porosity on mechanical and corrosion properties of SLM 316L stainless steel." Applied Physics A **128**(1).

Yang, N., J. Yee, B. Zheng, K. Gaiser, T. Reynolds, L. Clemon, W.-Y. Lu, J. Schoenung and E. Lavernia (2016). "Process-Structure-Property Relationships for 316L Stainless Steel Fabricated by Additive Manufacturing and Its Implication for Component Engineering." Journal of Thermal Spray Technology **26**.

Yang, Y., Y. Gong, C. Li, X. Wen and J. Sun (2020). "Mechanical performance of 316 L stainless steel by hybrid directed energy deposition and thermal milling process." Journal of Materials Processing Technology **291**: 117023.

Yu, J., M. Rombouts and G. Maes (2013). "Cracking behavior and mechanical properties of austenitic stainless steel parts produced by laser metal deposition." Materials & Design **45**: 228-235.

Zhang, B., S. Liu and Y. C. Shin (2019). "In-Process monitoring of porosity during laser additive manufacturing process." Additive Manufacturing **28**: 497-505.

Zhang, M., X. Zhou, D. Wang, L. He, X. Ye and W. Zhang (2022). "Additive manufacturing of in-situ strengthened dual-phase AlCoCuFeNi high-entropy alloy by selective electron beam melting." Journal of Alloys and Compounds **893**: 162259.

Zhang, Y., H. G. Soon, D. Ye, J. Y. H. Fuh and K. Zhu (2019). "Powder-bed fusion process monitoring by machine vision with hybrid convolutional neural networks." IEEE Transactions on Industrial Informatics **16**(9): 5769-5779.

Zhao, Y., M. N. Cinbiz, J.-S. Park, J. Almer and D. Kaoumi (2020). "Tensile behavior and microstructural evolution of a Fe-25Ni-20Cr austenitic stainless steel (alloy 709) from room to elevated temperatures through in-situ synchrotron X-ray diffraction characterization and transmission electron microscopy." Journal of Nuclear Materials **540**.

Zheng, B., J. Haley, N. Yang, J. Yee, K. W. Terrassa, Y. Zhou, E. Lavernia and J. M. Schoenung (2019). "On the evolution of microstructure and defect control in 316L SS components fabricated via directed energy deposition." Materials Science and Engineering: A **764**: 138243.

Zhi'En, E., J. Pang, J. Kaminski and H. Pepin (2018). "Characterisation of porosity, density, and microstructure of laser metal deposited Stainless Steel AISI 316L." Additive Manufacturing **25**.

Zhong, W., N. Sridharan, D. Isheim, K. G. Field, Y. Yang, K. Terrani and L. Tan (2021). "Microstructures and mechanical properties of a modified 9Cr ferritic-martensitic steel in the as-built condition after additive manufacturing." Journal of Nuclear Materials **545**.

Zhong, W., N. Sridharan, D. Isheim, K. G. Field, Y. Yang, K. Terrani and L. Tan (2021). "Microstructures and mechanical properties of a modified 9Cr ferritic-martensitic steel in the as-built condition after additive manufacturing." Journal of Nuclear Materials **545**: 152742.

Zhou, L., T. Yuan, R. Li, J. Tang, G. Wang, K. Guo and J. Yuan (2019). "Densification, microstructure evolution and fatigue behavior of Ti-13Nb-13Zr alloy processed by selective laser melting." Powder Technology **342**: 11-23.

Zhou, X., C. Liu, L. Yu, Y. Liu and H. Li (2015). "Phase Transformation Behavior and Microstructural Control of High-Cr Martensitic/Ferritic Heat-resistant Steels for Power and Nuclear Plants: A Review." Journal of Materials Science and Technology **31**: 235-242.

Ziętala, M., T. Durejko, M. Polański, I. Kunce, T. Płociński, W. Zieliński, M. Łazińska, W. Stępniowski, T. Czujko, K. J. Kurzydłowski and Z. Bojar (2016). "The microstructure, mechanical properties and corrosion resistance of 316L stainless steel fabricated using laser engineered net shaping." Materials Science and Engineering: A **677**: 1-10.

Pacific Northwest
National Laboratory

902 Battelle Boulevard
P.O. Box 999
Richland, WA 99354

1-888-375-PNNL (7665)

www.pnnl.gov